

Circumbinary discs for stellar population models

Robert G. Izzard^{1,2} and Adam S. Jermyn^{2,3}

¹*Astrophysics group, Department of Physics, University of Surrey, Guildford, GU2 7XH, United Kingdom.*

²*Institute of Astronomy, Madingley Road, Cambridge, CB3 0HA, United Kingdom.*

³*Center for Computational Astrophysics, Flatiron Institute, New York, NY 10010, USA.*

26th January 2024

ABSTRACT

We develop a rapid algorithm for the evolution of stable, circular, circumbinary discs suitable for parameter estimation and population synthesis modelling. Our model includes disc mass and angular momentum changes, accretion onto the binary stars, and binary orbital eccentricity pumping. We fit our model to the post-asymptotic giant branch (post-AGB) circumbinary disc around IRAS 08544-4431 finding reasonable agreement despite the simplicity of our model. Our best-fit disc has a mass of about $0.01 M_{\odot}$ and angular momentum $2.7 \times 10^{52} \text{ g cm}^2 \text{ s}^{-1} \approx 9 M_{\odot} \text{ km s}^{-1} \text{ au}$, corresponding to 0.0079 and 0.16 of the common-envelope mass and angular momentum respectively. The best-fit disc viscosity is $\alpha_{\text{disc}} = 5 \times 10^{-3}$ and our tidal torque algorithm can be constrained such that the inner edge of the disc $R_{\text{in}} \sim 2a$. The inner binary eccentricity reaches about 0.13 in our best-fitting model of IRAS 08544-4431, short of the observed 0.22.

The circumbinary disc evaporates quickly when the post-AGB star reaches a temperature of $\sim 6 \times 10^4 \text{ K}$, suggesting that planetismals must form in the disc in about 10^4 yr if secondary planet formation is to occur, while accretion from the disc onto the stars at ~ 10 times the inner-edge viscous rate can double the disc lifetime.

Key words: stars: AGB and post-AGB – stars: binaries: general – stars: winds, outflows – stars: circumstellar matter – planet-disc interactions – accretion, accretion discs

1 INTRODUCTION

Understanding the evolution of binary stars is vital to many areas of modern astrophysics. Phenomena that occur uniquely or primarily in binary systems include type Ia supernovae, X-ray binaries, thermonuclear novae, X-ray bursts, stellar rejuvenation and blue stragglers, the formation of stripped stars such as Wolf-Rayet and sdB/O stars, and the merging of stars with associated signals in gravitational waves and as kilonovae. Binary stars are thus fundamental to astrophysics, yet many aspects of their evolution remain poorly understood (De Marco & Izzard 2017).

Mass transfer is a vital process in binary-star evolution, and while Roche-lobe overflow as a basic concept is reasonably understood, quantitative details regarding efficiency of mass transfer are not yet pinned down. Transferred material can be retained by the companion star or lost from the system, and the fate of associated angular momentum is equally uncertain. Because the specific angular momentum of transferred material is often large compared to the associated stellar specific angular momentum, discs form in many mass-transferring binaries. These discs can be either circumstellar, around one or both stars, or circumbinary, around the binary as a whole. From observations we know that, at least in some binaries, a disc forms outside the binary orbit in a circumbinary disc (Kervella et al. 2016; Haworth et al. 2018). The circumbinary disc material may have been ejected by a wind from its parent star, or during non-conservative mass transfer or common-envelope ejection (e.g. Kashi & Soker 2011). A better understanding of the formation and

evolution of such discs, and their interaction with their binary parent stars, is the aim of this paper.

Binary post-giant branch (post-GB) and post-asymptotic giant branch (post-AGB) stars (together referred to below as post-(A)GB) are a class of systems which are observed to have surrounding discs (Bujarrabal et al. 2013), indeed *all* post-AGB systems with discs are binaries. These binaries contain a relatively hot ($\gtrsim 6 \times 10^3 \text{ K}$), bright, compact object which has just left the AGB and a usually main-sequence dwarf companion star. The post-AGB star has a compact degenerate core surrounded by a thin envelope containing about $10^{-3} M_{\odot}$ of mostly hydrogen. At the interface of the core and envelope is a hydrogen-burning shell which generates the typically $10^4 L_{\odot}$ luminosity of the system.

The circumbinary discs in post-AGB systems are mostly Keplerian and stable (de Ruyter et al. 2006; Gallardo Cava et al. 2021). Their masses are up to $10^{-2} M_{\odot}$, with outer diameters of about $10^5 R_{\odot}$ and angular momenta up to $10^{52} \text{ g cm}^2 \text{ s}^{-1}$ which is similar to their inner binary system. Mass loss is observed from the outer part of the disc, which can be sub-Keplerian, and inflow at the inner edge onto the binary stars is observed at rates up to $10^{-7} M_{\odot} \text{ yr}^{-1}$ (Bujarrabal et al. 2018). Material that flows inward is poor in metals because these are lost in a dusty outflow, thus the surface of the post-AGB star is polluted with low-metallicity material (Oomen et al. 2020). This accretion may also prolong the life of the post-AGB star and circumbinary disc, and hence increase the number of post-AGB binaries relative to the equivalent single stars.

The orbits of post-AGB stars with circumbinary discs have periods

ranging from tens to thousands of days (Oomen et al. 2018). While the wide systems, with periods longer than about 1000 d, may form circumbinary discs from wind material ejected during the previous AGB phase (Saladino & Pols 2019), systems with shorter periods probably passed through a phase of Roche-lobe overflow followed by common-envelope evolution because their orbits are too small to contain an AGB star of radius $\sim 500 R_{\odot}$ (Izzard et al. 2012; Ivanova et al. 2013). During common-envelope evolution, the AGB core and its companion transfer orbital energy and angular momentum into the envelope and thus eject it. Evolved AGB stars are poorly bound (Wang et al. 2016), so only a little energy is required from the orbit for envelope ejection, and hence the orbit also shrinks little during this phase.

The circumbinary disc interacts with its binary system through both mass accretion and resonant interactions that may increase the eccentricity of the binary orbit. Post-AGB systems with periods shorter than 1000 d should be circular because of efficient tidal dissipation, and yet many are observed to have eccentricities up to $e = 0.4$, and a few have $e \gtrsim 0.6$ (Oomen et al. 2018). Resonant interactions have been explored as sources of this eccentricity previously, but the models employed were either rather limited in that they assumed a fixed disc mass and lifetime (Dermine et al. 2013), or did not include feedback with stellar evolution and subsequent disc evaporation (Rafikov 2016a). The magnitude of eccentricity pumping depends crucially on both the disc lifetime and mass.

Recent interest in circumbinary planets, of which about a dozen are now known (e.g. Kley & Haghighipour 2015; Getley et al. 2017), naturally leads to speculation that these may form in evolved stellar systems with circumbinary discs. Post-AGB binaries are prime candidates for such planet formation given that they host apparently stable circumbinary discs. Understanding post-AGB circumbinary discs is thus key to also knowing whether they are important sources of planets or other rocky objects that may form debris discs around their offspring (Chachan et al. 2019; Yelverton et al. 2019). Many other close-binary formation channels may also be influenced by circumbinary discs. For example, Chen & Podsiadlowski (2019) investigate the influence of a circumbinary disc on the formation and evolution of X-ray binaries originating from red supergiant systems.

In the following we develop a circumbinary-disc model that is fast enough to be suitable for stellar population synthesis modelling yet incorporates the physics required to study the interaction of a circumbinary disc with its inner binary star system and the interstellar medium. Our model makes reasonable approximations to facilitate fast computation yet allows predictions of system properties for comparison with observations to pin down uncertain physics. In Sec. 2 we develop our circumbinary-disc model. Sec. 3 explores interaction between the disc and its inner binary system. Sec. 4 models the disc recently observed by the Atacama Large Millimeter Array (ALMA), IRAS 08544-4431 (Bujarrabal et al. 2018). In Sec. 5 we discuss relevant uncertainties, and the limitations and successes of our model. We then conclude.

2 CIRCUMBINARY DISC MODEL

We require a fast circumbinary disc model for application in population synthesis calculations of millions of binary-star systems covering a many-parameter space (Izzard & Halabi 2018) and, in this paper, to model the disc in the system IRAS 08544-4431. Given the many uncertainties involved, and our requirement for speed of model execution, we adopt a semi-analytic model guided by observed post-AGB circumbinary discs. Our model is conservative, in that it assumes

the discs to be in equilibrium and changing slowly relative to their viscous timescale.

These circumbinary discs are almost Keplerian (de Ruyter et al. 2006) and, with observed mass loss rates of $10^{-7} M_{\odot} \text{ yr}$ and masses of about $10^{-2} M_{\odot}$, are stable on time-scales of at least $10^4 - 10^5 \text{ yr}$. This is long compared to the viscous time-scale at the inner edge of the disc, which is typically 10^3 yr or shorter. We thus assume that viscous spreading of the disc (cf. Lynden-Bell & Pringle 1974) is fast, such that the angular momentum flux in the disc adjusts instantly to changes in the disc structure and binary torque. This allows us to treat mass loss as just changing the total mass of the disc, rather than having to track precisely from where the mass comes and how the disc spreads to restore equilibrium. These assumptions, and our approach of using matched power-law solutions (Sec. 2.3), are in the spirit of (Shakura & Sunyaev 1973), Phinney & Hansen (1993) and Haiman et al. (2009), though with a somewhat different physical setup. Our disc is split into matched power-law zones depending on which term in the energy equation (Eq. 16) dominates under our assumptions of only gas pressure and constant opacity, whereas in, e.g., Shakura & Sunyaev (1973) and Haiman et al. (2009) the splits are based on the dominant opacity and pressure source.

Our assumptions are valid at the inner edge of our discs, where the density is greatest and interaction with the inner binary is strongest, but often not at the outer edge as we discuss in Sec. 5.1. We find in practice that mass loss barely affects the structure of the disc except during its evaporation (Sec. 3.2), at which point the disc is completely disrupted in a few years. Such fast evolutionary phases are rarely observed, so our model is appropriate for comparison with most observed, circumbinary, post-AGB discs.

2.1 Disc formation

We form circumbinary discs in binary systems when a common envelope is ejected. The disc mass, M_{disc} , is a fraction, f_M , of the ejected common-envelope mass, M_{CE} , such that,

$$M_{\text{disc}} = f_M M_{\text{CE}}. \quad (1)$$

The disc is given an angular momentum, J_{disc} , that is a fraction of the angular momentum in the common envelope, J_{CE} ,

$$J_{\text{disc}} = f_J J_{\text{CE}}. \quad (2)$$

We require $0 \leq f_M < 1$, to conserve mass, and $0 \leq f_J < 1$ as we do not expect common-envelope evolution to leave a retrograde central binary. Typically $f_M \ll 1$ and $f_J \ll 1$, although we do not additionally require $f_M = f_J$. While we are theoretically free to choose f_J thus, too much or too little angular momentum leads to immediate partial or full evaporation of the disc (Sec. 3.2). Such objects are not candidate post-AGB discs. We also require that $M_{\text{disc}} \ll M_1 + M_2$, where M_1 and M_2 are the masses of the stars in the binary system, such that the disc is gravitationally stable. Given the observed masses of post-AGB discs are about $0.01 M_{\odot}$ or less, and that post-AGB binaries have masses of about $1 M_{\odot}$, this is never a problem.

As an example, consider a circular binary system with, prior to mass transfer, $M_1 = 1.5 M_{\odot}$, $M_2 = 0.9 M_{\odot}$ and orbital separation $a_{\text{bin}} = 800 R_{\odot}$ corresponding to an orbital period $P_{\text{bin}} \approx 1700 \text{ d}$. The orbital separation is chosen such that Roche-lobe overflow starts during the thermally-pulsing asymptotic giant branch (TPAGB) and leads to common-envelope evolution. The orbital angular momentum at this time is about $1.3 \times 10^{53} \text{ g cm}^2 \text{ s}^{-1}$. Assuming efficient common-envelope ejection, about $0.6 M_{\odot}$ is ejected, so with $f_M = 1.8 \text{ per cent}$ and $f_J = 15 \text{ per cent}$ we have a disc with mass $M_{\text{disc}} = 0.013 M_{\odot}$ and angular momentum $J_{\text{disc}} = 1.25 \times 10^{52} \text{ g cm}^2 \text{ s}^{-1}$,

similar to both observed post-AGB discs and the formation scenario proposed by [Kashi & Soker \(2011\)](#).

2.2 Disc structure

We assume material in the circumbinary disc is on circular orbits around the centre of mass of the binary-star system and is in a Keplerian steady state. We model only gas in the disc, neglecting dust, because most of the mass in the disc is expected to be in the gas phase. We assume the disc is thin, i.e. $H(R) \ll R$ where $H(R)$ is the scale height at radius R from the centre of mass. That we are in a steady state implies we can neglect time derivatives, and hence the temperature structure of the disc is given by solutions to the energy conservation equation,

$$\sigma T^4 = \mathcal{A} + \mathcal{B}(1 + C) + \mathcal{D}, \quad (3)$$

where $T = T(R)$ is the mid-plane temperature of the disc at radius R and σ is the Stefan-Boltzmann constant. [Perets & Kenyon \(2013\)](#) derive these terms in detail (see also [King 1998](#)), but briefly they include a viscous heating term,

$$\mathcal{A} = \frac{27\kappa\nu\Sigma^2\Omega^2}{64}, \quad (4)$$

where,

$$\Omega = \Omega(R) = \sqrt{\frac{G(M_1 + M_2)}{R^3}}, \quad (5)$$

is the Keplerian angular velocity at radius R , $\Sigma = \Sigma(R)$ is the mass column density at radius R (Sec. 2.3.1), $\kappa = \kappa(R)$ is the opacity, $\nu = \nu(R)$ is the kinematic viscosity (Eq. A5) and G is the gravitational constant. Irradiation from the central star leads to the heating term,

$$\mathcal{B} = \frac{2F_\star}{3\pi} \left(\frac{R_\star}{R}\right)^3, \quad (6)$$

where,

$$F_\star = \frac{(L_1 + L_2)}{4\pi R_\star^2}, \quad (7)$$

is the incident luminous stellar flux with corresponding flux-weighted stellar radius,

$$R_\star = \frac{F_1 R_1^3 + F_2 R_2^3}{F_1 R_1^2 + F_2 R_2^2}, \quad (8)$$

with F_i and R_i the flux and radius of star $i = 1, 2$. The disc geometry is encoded in,

$$C = \frac{3\pi H}{4R_\star} \left(\frac{\partial \ln H}{\partial \ln R} - 1\right) \quad (9)$$

and mass loss in,

$$\mathcal{D} = \frac{G(M_1 + M_2)}{2\pi a} \dot{M} R^{-2}, \quad (10)$$

where a is the binary separation and $\dot{M} = \dot{M}(R)$ is the mass loss rate at radius R .

In the following, we set $\mathcal{D} = 0$ and thus ignore mass loss (or gain) as a sink (or source) of energy in our discs. We test this assumption in Appendix E and find it to be good within 10 per cent. We are then left to solve,

$$\sigma T^4 = \mathcal{A} + \mathcal{B}(1 + C), \quad (11)$$

and we proceed by writing \mathcal{A} , \mathcal{B} and C in terms of the radius R ,

temperature $T = T(R)$ and a multiplier. The local sound speed is, assuming an ideal-gas equation of state,

$$c_s(R) = \sqrt{\frac{\Gamma k_B T}{\mu}}, \quad (12)$$

and the local scale height is,

$$H(R) = \frac{c_s(R)}{\Omega(R)} = \sqrt{\frac{\Gamma k_B}{\mu G(M_1 + M_2)}} T^{1/2} R^{3/2}, \quad (13)$$

where Γ is the adiabatic index of the gas in the disc (neutral hydrogen gas has $\Gamma = 1.4$), k_B is the Boltzmann constant and μ is the mass of the gas particles in the disc. Differentiating Eq. 13 by R , we find,

$$\frac{\partial \ln H}{\partial \ln R} = \frac{1}{2} \frac{\partial (\ln T + 3 \ln R)}{\partial \ln R} = \frac{1}{2} \frac{\partial \ln T}{\partial \ln R} + \frac{3}{2}. \quad (14)$$

The kinematic viscosity is,

$$\nu(R) = \frac{\alpha_{\text{disc}} c_s^2}{\Omega} = \frac{\alpha_{\text{disc}} \Gamma k_B T}{\mu} \sqrt{\frac{R^3}{G(M_1 + M_2)}}, \quad (15)$$

where we assume a constant disc viscosity parameter, α_{disc} ([Shakura & Sunyaev 1973](#)). Combining Eqs. 3, 5, 7, 8, 14 and 15, and dividing by σ we find,

$$T^4 = a \Sigma^2 T R^{-3/2} + b T^{1/2} R^{-3/2} + c R^{-3}, \quad (16)$$

where

$$a = \frac{27\kappa\alpha_{\text{disc}}\Gamma k_B \sqrt{G(M_1 + M_2)}}{64\sigma\mu}, \quad (17)$$

$$b = \frac{F_\star R_\star^2}{4\sigma} \sqrt{\frac{\Gamma k_B}{\mu G(M_1 + M_2)}} \left(1 + \frac{\partial \ln T}{\partial \ln R}\right) \approx \frac{F_\star R_\star^2}{4\sigma} \sqrt{\frac{\Gamma k_B}{\mu G(M_1 + M_2)}} \quad (18)$$

and

$$c = \frac{2F_\star R_\star^3}{3\pi\sigma}. \quad (19)$$

2.3 Solution method

We implement our disc-solution method in the `BINARY_C` code so that disc and binary-system evolution are coupled from the moment of disc formation to its evaporation. In our model the disc is fully specified by giving its mass and angular momentum. `BINARY_C` can then reconstruct profiles of quantities in the disc as required. Hence, we feed `BINARY_C` the initial mass and angular momentum, and then it constructs the disc and evolves it forward in time. At every `BINARY_C` timestep, to solve Eq. 16 throughout the disc we calculate the terms multiplied by a , b and c , neglect the smallest two, substitute Eq. 20 and solve the resulting expression. This gives us a power law relating temperature and radius, $\log T \propto \log R$. For these purposes we neglect the term $\partial \ln T / \partial \ln R$ in Eq. 18 because in the region where \mathcal{B} dominates this evaluates to a constant smaller than unity.

We define zones of the disc to be the regions in which one of the a , b or c terms in Eq. 16 is largest. In each zone we then neglect the two smaller terms leaving a unique temperature-radius power-law relation, $T(R)$, in the zone. Zones must have radii that satisfy $R_{\text{in}} \leq R \leq R_{\text{out}}$ to be considered part of the disc.

Our calculated $T(R)$ is most erroneous at the edges of the zones. In the worst case scenario the maximum error in T^4 is a factor 3 because there are at most two terms we have neglected, each of which is at

most equal in magnitude to the dominant one in the zone. It follows that the maximum error in $T(R)$ is $3^{1/4} - 1 \approx 32$ per cent. This is the same magnitude of error as in of [Phinney & Hansen \(1993\)](#) and [Haiman et al. \(2009\)](#), and is characteristic of matched-power law solutions.

We show in Appendix E that the maximum error in $T(R)$ our IRAS 08544-4431 model is 20 per cent. Given the uncertainties in the parameters used to construct the disc, such as mass and viscosity which are known only to order-of-magnitude at best, the speed advantage of our solution method compared to more complicated, albeit more precise, methods makes it ideal for modelling the large binary-star parameter space.

2.3.1 Mass scaling

The term $\Sigma(R)$ is related to the angular momentum flux through the disc \mathcal{F} by,

$$\Sigma(R) = \frac{\mathcal{F}}{3\pi h v}, \quad (20)$$

where,

$$h = h(R) = \sqrt{G(M_1 + M_2)R}, \quad (21)$$

is the specific angular momentum at radius R and \mathcal{F} is defined in Eq. B6. By combining this with Eq. 15, we have,

$$\Sigma(R) = \left(\frac{\mathcal{F}\mu}{3\pi\alpha_{\text{disc}}\Gamma k_B} \right) T^{-1} R^{-2} = \Sigma_0 T^{-1} R^{-2}, \quad (22)$$

which defines Σ_0 ,

$$\Sigma_0 = \Sigma(R) T R^2 = \frac{\mathcal{F}\mu}{3\pi\alpha_{\text{disc}}\Gamma k_B}. \quad (23)$$

The mass of the disc is set by choosing Σ_0 appropriately as described in Sec. 2.5.

2.3.2 Temperature power law $T(R)$

By combining Eqs. 16 and 22, we select the temperature as a function of radius according to the dominant term in Eq. 16,

$$T(R) = \zeta R^\eta = \max\left(AR^{-11/10}, BR^{-3/7}, CR^{-3/4}\right). \quad (24)$$

The coefficients A, B, C , hence ζ and η , are given in Table 1. We then write the temperature power law in zone n , which extends from radii $R_{0,n}$ to $R_{1,n}$ (Eq. 26), with exponent a_n as,

$$T_n(R) = T_{0,n} \left(\frac{R}{R_{0,n}} \right)^{a_n}, \quad (25)$$

where $T_{0,n}$ is the temperature at the inner edge and $T_n(R_{1,n})$ is the temperature at the outer edge of the zone.

2.3.3 General power laws

Physical quantities throughout the disc are expressed as power law functions of radius, R . Our discs have N zones labelled $n = 0 \dots N-1$ where $N \leq 3$. A quantity $A_n(R)$ in zone n is represented by a power law in R ,

$$A_n(R) = A_{0,n} \left(\frac{R}{R_{0,n}} \right)^{b_n} = A_{0,n} R_{0,n}^{-b_n} R^{b_n}, \quad (26)$$

where $R_{0,n}$ and $R_{1,n}$ are the inner and outer radii of zone n such that in the zone $R_{0,n} \leq R \leq R_{1,n}$, $A_{0,n} = A_n(R_{0,n})$ and $A_{1,n} = A_n(R_{1,n})$

are the quantity at the inner and outer radius of zone n , respectively, and b_n is the exponent of the power law in zone n . The power-law exponent can be written,

$$b_n = m a_n + c, \quad (27)$$

where m and c are constants, and a_n is the temperature power-law exponent (Table 1). (Table 1). Each physical quantity of interest can thus be defined by the two constants m and c .

The power laws are continuous across zone boundaries. Crossing radii, $R_{x,i,j}$, between zones i and j satisfy,

$$A_{0,i} \left(\frac{R_{x,i,j}}{R_{0,i}} \right)^{b_i} = A_{0,j} \left(\frac{R_{x,i,j}}{R_{0,j}} \right)^{b_j}, \quad (28)$$

hence

$$R_{x,i,j} = \left(\frac{A_{0,i} R_{0,j}^{b_j}}{A_{0,j} R_{0,i}^{b_i}} \right)^{\frac{1}{b_j - b_i}}. \quad (29)$$

As an example, the surface density $\Sigma(R)$ is, from Eq. 22, given by,

$$\begin{aligned} \Sigma(R) &= \Sigma_0 \times T_{0,n}^{-1} \left(\frac{R}{R_{0,n}} \right)^{-a_n} \times R_{0,n}^{-2} \left(\frac{R}{R_{0,n}} \right)^{-2} \\ &= \Sigma_0 T_{0,n}^{-1} R_{0,n}^{-2} \left(\frac{R}{R_{0,n}} \right)^{-a_n - 2} \\ &= \Sigma(R_{0,n}) \left(\frac{R}{R_{0,n}} \right)^{-a_n - 2}, \end{aligned} \quad (30)$$

which is a general power law with $m = -1$ and $c = -2$ (Eq. 27). Further physical quantities are given in Appendix A.

2.4 Integrated quantities

Integrated properties of the disc, such as its total mass, luminosity and angular momentum, are constructed from our power-law solutions. The total integral, I , over the disc is the sum of the partial integrals, I_n , in its zones,

$$I = \sum_{n=0}^{N-1} I_n. \quad (31)$$

We can write each integral using an integrand function, $i_n(R)$, which is also a power law in R ,

$$i_n(R) = i_{0,n} \left(\frac{R}{R_{0,n}} \right)^{b_n}, \quad (32)$$

hence over a single zone,

$$I_n = \int_{R_{0,n}}^{R_{1,n}} i_n(R) dR \quad (33)$$

$$= i_{0,n} \int_{R_{0,n}}^{R_{1,n}} \left(\frac{R}{R_{0,n}} \right)^{b_n} dR \quad (34)$$

$$= \frac{i_{0,n}}{1 + b_n} R_{0,n}^{-b_n} \left(R_{1,n}^{1+b_n} - R_{0,n}^{1+b_n} \right), \quad (35)$$

such that the total integral is,

$$I = \sum_{n=0}^{N-1} \frac{i_{0,n}}{1 + b_n} R_{0,n}^{-b_n} \left(R_{1,n}^{1+b_n} - R_{0,n}^{1+b_n} \right). \quad (36)$$

In the n th zone only the constants $i_{0,n}$ and b_n are required to calculate the integrals i_n and hence the total integral I . In general we can then write,

$$b_n = c a_n + m, \quad (37)$$

Table 1. Temperature, T , power law prefactors, ζ , and slope exponents, η , where $T = \zeta R^\eta$ inside the disc and R is the distance to the centre of the system.

Power law	Prefactor	Exponent	Physical process
A	$A = a^{1/5} \Sigma_0^{-2/5} = \left(\frac{27\kappa \alpha_{\text{disc}} \Gamma k_B \sqrt{GM_\star}}{64\sigma\mu} \right)^{1/5} \Sigma_0^{-2/5}$	-11/10	Viscous Heating
B	$B = b^{2/7} = \left(\frac{F_\star R_\star^2}{7\sigma} \sqrt{\frac{\Gamma k_B}{\mu GM_\star}} \right)^{2/7}$	-3/7	Irradiation (Bare Term)
C	$C = c^{1/4} = \left(\frac{2F_\star R_\star^3}{3\pi\sigma} \right)^{1/4}$	-3/4	Irradiation (Slope Correction)

such that integral properties of the disc each correspond to a choice of the constants c and m .

2.4.1 Total disc mass M_{disc}

The total mass of the disc is,

$$M_{\text{disc}} = \int_{R_{\text{in}}}^{R_{\text{out}}} dM = \int_{R_{\text{in}}}^{R_{\text{out}}} 2\pi R \Sigma(R) dR \quad (38)$$

$$= \sum_{n=0}^{N-1} \int_{R_{0,n}}^{R_{1,n}} 2\pi R_{0,n} \left(\frac{R}{R_{0,n}} \right) \Sigma(R_{0,n}) \left(\frac{R}{R_{0,n}} \right)^{-2-a_n} dR \quad (39)$$

$$= \sum_{n=0}^{N-1} [2\pi R_{0,n} \Sigma(R_{0,n})] \int_{R_{0,n}}^{R_{1,n}} \left(\frac{R}{R_{0,n}} \right)^{-1-a_n} dR, \quad (40)$$

The integrand is in the form of Eq. 36 with,

$$b_n = -a_n - 1 = ca_n + m, \quad (41)$$

where,

$$c = m = -1, \quad (42)$$

and $i_n = 2\pi R_{0,n} \Sigma(R_{0,n})$ (Eq. 30).

2.4.2 Further integrals

Similarly to above, further global disc properties can be written in this integral form, including the angular momentum, angular momentum flux, luminosity, moment of inertia, and the potential and kinetic energies of the disc. Appendix B derives them in full while table 2 lists the parameters c and m to be used in Eqs. 36 and 37. Quantities such as the half-mass and half-angular momentum radii are found by using the above method with bisection on a variable upper limit in the integral.

2.5 Constructing the disc

We have three parameters in our circumbinary disc model: the surface density scaling factor Σ_0 , the inner radius R_{in} and the outer radius R_{out} . We have three constraints: the disc mass M_{disc} , the disc angular momentum J_{disc} and the disc angular momentum flux \mathcal{F} which is related to the resonant torque exerted by the inner binary on the disc (Sec. 3.3 and Appendix B). We employ the *GNU Scientific Library* MULTIROOT solvers to find the appropriate Σ_0 , R_{in} and R_{out} given M_{disc} , J_{disc} and \mathcal{F} to typically one part in 10^6 . On the rare occasion that this method fails, we revert to a slower bisection method and then resume with the MULTIROOT solvers.

3 DISC–BINARY INTERACTION

A key aspect of our model is its ability to describe the changes in a circumbinary disc and its inner binary as time progresses. We combine a rapid stellar population code with our disc model to achieve this with the immediate goal of modelling the disc around IRAS 08544-4431.

3.1 Stellar evolution and mass loss

We evolve binary systems using `BINARY_C`, a rapid stellar evolution and nucleosynthesis code originally based `BSE` of Hurley et al. (2002) with modifications as described in Izzard et al. (2004, 2006, 2009, 2018). `BINARY_C` calculates the stellar luminosity, radius, temperature, core mass and wind-loss rates of stars in the binary as a function of time and models mass transfer by winds and Roche-lobe overflow. Systems which undergo unstable mass transfer enter a common-envelope phase, which is described by the energy-balance prescription of Hurley et al. (2002, their Sec. 2.7.1). The parameter α_{CE} is the fraction of the orbital energy that is available to eject the common envelope. We set $\alpha_{\text{CE}} = 1$ by default. The parameter λ_{CE} describes the binding energy of the envelope as a function of its mass and radius (Hurley et al. 2002), and is calculated based on the models of Dewi & Tauris (2000). The envelopes of TPAGB stars are poorly bound compared to other stages of stellar evolution, so λ_{CE} is often large, sometimes as much as 100, and hence the envelope is easily ejected and merging systems – when ejection fails – are rare. A fraction f_{ion} , by default 10 per cent, of the envelope’s recombination energy is assumed to aid its ejection resulting in efficient envelope ejection from TPAGB stars with little orbital shrinkage.

Our common-envelope prescription differs from Hurley et al. (2002) in that we do not assume the post-common envelope object is a fully-stripped white dwarf with no hydrogen envelope. Instead, we leave enough mass in the post-AGB envelope that it 95 per cent fills its Roche-lobe. Typically this mass is about $10^{-2} M_\odot$. Hydrogen burning and mass loss erode the hydrogen envelope as the star moves blueward in the Hertzsprung-Russell diagram. The star becomes a white dwarf once its hydrogen envelope is gone, and it then evolves along a canonical white dwarf cooling track. In our binaries there is the possibility of mass accretion onto the stars from the inner edge of the circumbinary disc. This slows blueward progress of the star by replenishing the stellar hydrogen envelope (Sec. 5.3).

Our stellar wind prescription follows that of Hurley et al. (2002), where the Vassiliadis & Wood (1993) wind is most important on the AGB and the Nieuwenhuijzen & de Jager (1990) Wolf-Rayet wind activates during the hot post-AGB phase. We discuss the impact of this choice in Secs. 3.4 and 5.3.

Table 2. Integrand parameters which should be applied in Eq. 36 to calculate the integrated properties of our circumbinary discs as listed in the first column. The prefactors depend on properties of the inner binary and the temperature $T(R_{0,n})$, surface mass density $\Sigma(R_{0,n})$ and radii $R_{0,n}$ at the inner edge of the n th zone in the disc.

Integral	Symbol	c	m	Prefactor $i_{0,n}$
Mass	M_{disc}	-1	-1	$2\pi R_{0,n} \Sigma(R_{0,n})$
Angular momentum	J_{disc}	$-\frac{1}{2}$	-1	$2\pi \sqrt{GM_b} R_{0,n}^{3/2} \Sigma(R_{0,n})$
Angular momentum flux	\mathcal{F}	-6	-1	$f_{\text{tid}} \pi a^4 q^2 GM_b \Sigma(R_{0,n}) R_0^{-4}$
Luminosity	L_{disc}	1	4	$4\pi \sigma T_{0,n}^4 R_{0,n}$
Moment of inertia	I_{disc}	1	-4	$2\pi R_0^3 \Sigma(R_{0,n})$
Gravitational potential energy	$E_{\text{disc,grav}}$	-2	-1	$\pi GM_b \Sigma(R_{0,n})$
Kinetic energy	$E_{\text{disc,kin}}$	-2	-1	$-2\pi GM_b \Sigma(R_{0,n})$

3.2 Disc mass loss

We treat mass changes to the disc as either a fast phenomenon that changes the disc instantaneously, or as a slow change that does not affect the disc structure, i.e. Eq. 10 is small compared to Eqs. 4, 6 and 9. The mass and angular momentum of the circumbinary disc then evolve according to,

$$\dot{M}_{\text{disc}} = \dot{M}_{\text{slow}} + \dot{M}_{\text{fast}}, \quad (43)$$

$$J_{\text{disc}} = J_{\text{slow}} + J_{\text{fast}}, \quad (44)$$

with slow mass-loss and angular-momentum-loss rates given by,

$$\dot{M}_{\text{slow}} = \dot{M}_{\text{visc}} + \dot{M}_{\text{wind}}, \quad (45)$$

and

$$J_{\text{slow}} = J_{\text{visc}} + J_{\text{wind}} + J_{\text{torque}}, \quad (46)$$

respectively, and their fast (i.e. instantaneous) equivalents,

$$\dot{M}_{\text{fast}} = \dot{M}_{\text{inner}} + \dot{M}_{\text{ram}}, \quad (47)$$

and

$$J_{\text{fast}} = J_{\text{inner}} + J_{\text{ram}}. \quad (48)$$

The terms in Eqs. 43 to 48 are described below.

3.2.1 Slow mass changes, \dot{M}_{slow}

The slow terms, \dot{M}_{slow} and J_{slow} , are applied to the disc every timestep. Inflow onto the central binary from the inner edge of the disc is at a viscous rate,

$$\dot{M}_{\text{visc}} = -3\pi f_{\text{visc}} \nu(R_{\text{in}}) \Sigma(R_{\text{in}}), \quad (49)$$

where $f_{\text{visc}} \approx 1$ is a parameter. We show in Sec. 4.3 that the time-scale for the disc to evaporate by this method is an order of magnitude longer than the disc lifetime and many orders of magnitude longer than the binary orbit. Accreted gas takes a fraction of its angular momentum with it onto the inner binary, i.e.,

$$J_{\text{visc}} = f_{\text{visc},J} h_{\text{visc}} \dot{M}_{\text{visc}}, \quad (50)$$

with $h_{\text{visc}} = h(R_{\text{in}})$ and $f_{\text{visc},J} \approx 1$. Sec. 3.3 describes accretion onto the stars.

Radiation, particularly far-ultraviolet and X-ray, from the inner binary penetrates the disc and launches a wind from its surface. The rate of mass loss, \dot{M}_{wind} , and associated rate of angular momentum loss, J_{wind} , are calculated by integrating Eq. B5 of Appendix B2 in Owen et al. (2012) over the disc modulated by a parameter $f_X \approx 1$. The X-ray luminosity of the central stars, L_X , is calculated assuming

they are black bodies and X-rays have energies in the range 0.1 – 100 keV.

The resonant torque, J_{torque} , is described in Sec. 3.3. We also adjust the angular momentum flux, \mathcal{F} to account for the lost material (the appropriate integral is given in Appendix B3).

3.2.2 Fast mass loss, \dot{M}_{fast}

Processes that act on timescales typically shorter than the disc viscous time-scale are grouped into a mass-loss rate, \dot{M}_{fast} , and associated angular momentum loss rate, J_{fast} .

The disc is instantaneously stripped at the outer edge by interaction with the interstellar medium if the disc is large enough. Given an interstellar medium pressure $P_{\text{ISM}} = 3000 k_B \text{ K}^{-1}$ (Cox 2005) we find the radius, R , at which $P(R) = P_{\text{ISM}}$ and remove mass and angular momentum outside this radius. In our models of IRAS 08544-4431, this radius lies outside the disc so ram-pressure stripping is never experienced.

Similarly, if the disc is small enough to be very close to the Roche lobes, i.e. $R_{\text{in}} < a_{L2}$, where a_{L2} is the second Lagrange-point radius, we strip material inside a_{L2} and remove its mass and angular momentum. Our IRAS 08544-4431 model contains sufficient angular momentum to avoid this.

3.2.3 Coupled mass loss

When mass is lost by photoevaporation at either edge of the disc we provide the option, enabled by default, to strip the disc to the radius at which the mass-loss time-scale equals the local viscous time-scale. This is necessary because if the mass loss is faster than viscous spreading, the disc cannot expand to quickly replace the lost mass, which is one of our main assumptions in constructing the disc. Typically in such cases the whole disc evaporates in a few years, although for our model of IRAS 08544-4431 turning this option off makes negligible difference.

3.3 Binary interaction

Mass is accreted onto stars 1 and 2 at rates,

$$\dot{M}_1 = f_q \dot{M}_{\text{visc}}, \quad (51)$$

and

$$\dot{M}_2 = (1 - f_q) \dot{M}_{\text{visc}}, \quad (52)$$

respectively, where f_q is set by either $f_q = 0.5q$ (Young & Clarke 2015, our default choice), $f_q = q/(1 + q)$ (Gerosa et al. 2015)

or $f_q = 0.5$, and $q = M_2/M_1$. The mass carries specific angular momentum $h_{\text{visc}} = f_{\text{visc},J} h(R_{\text{in}})$ (Eq. 50) onto the inner binary, where $f_{\text{visc},J} = 0.6$ by default based on the suggestion of Muñoz et al. (2019) that we should use $f_{\text{visc},J} = 0.4-0.8$, although this parameter may also exceed 1 according to their Fig. 3. Note, however, that jet formation may reduce accretion even further and we do not model this (cf. Soker 2019). In any case, observed post-(A)GB binaries have orbital periods of 100 – 1000 d with $J_{\text{orb}} \approx 10^{52} \text{ g cm}^2 \text{ s}^{-1}$. If the whole circumbinary disc is accreted without any loss of material, J_{orb} changes by at most a fraction $f_j \ll 1$ with a correspondingly small change in orbital period and separation. Accretion onto the stars, and associated spin up, is treated similarly to Roche-lobe overflow in BSE and BINARY_C (Hurley et al. 2002 and Sec. 3.4).

The torque imparted on the disc by the binary, \dot{J}_{torque} , is calculated by integrating the specific torque of Armitage & Natarajan (2002) over the disc assuming it is thin and larger than the binary orbit, i.e. $R > a$,

$$\Lambda(R) = \frac{1}{2} f_{\text{tid}} a^4 q^2 G M_{\text{binary}} R^{-5}, \quad (53)$$

where the multiplier $f_{\text{tid}} \approx 10^{-3}$ is a parameter. This choice for f_{tid} puts the inner edge of the disc at about $2a$, but R_{in} can be increased by increasing f_{tid} should the inner edge be at larger radius, e.g. at the inner dust edge (Deroo et al. 2007).

We pump the binary eccentricity, e , according to the prescription of Dermine et al. (2013) for which,

$$\frac{\dot{a}_{\text{res}}}{a} = -2 f_{\text{res}} \frac{l}{m} \alpha_{\text{disc}} a \Omega_b R_{J1/2}^{3/2} \frac{M_{\text{disc}}(M_1 + M_2)}{M_1 M_2}, \quad (54)$$

where $l = 1$, $m = 2$, Ω_b is the orbital angular frequency of the binary and $f_{\text{res}} \approx 1$ is a parameter. The half-angular momentum radius, $R_{J1/2}$, is the radius that contains half the disc's angular momentum and is found by bisection (Sec. 2.4.2). The eccentricity pumping rate is then,

$$\dot{e}_{\text{res}} = 2e g_R \frac{\dot{a}_{\text{res}}}{a} \times \begin{cases} -25\alpha_{\text{disc}}^{-1} & e < 0.1\sqrt{\alpha_{\text{disc}}}, \\ 0 & e > 0.7, \\ \left(\frac{1-e^2}{e^2+0.01\alpha_{\text{disc}}}\right) \left(\frac{l}{m} - \frac{1}{\sqrt{1-e^2}}\right) & \text{otherwise.} \end{cases} \quad (55)$$

The factor,

$$g_R = \min\left(\frac{2a}{R_{\text{in}}}, 1\right)^3, \quad (56)$$

reduces the rate of eccentricity pumping when R_{in} moves outside the $l = 1$, $m = 2$ resonance. Dermine et al. (2013) assume $R_{\text{in}} = 2a$, i.e. $g_R = 1$.

Despite its simplicity, the above formalism agrees reasonably with modern hydrodynamic simulations (Fleming & Quinn 2017). We ignore eccentricity pumping caused by accretion of material onto the binary because Oomen et al. (2020) find its effect, based on the results of Muñoz et al. (2020), to be negligible.

3.4 Post-(A)GB and binary evolution

The luminosity of the post-(A)GB star is set by its core mass, where we use the fitting formulae of Hurley et al. (2002, their Sec. 2.7.1) during the first giant branch and early-AGB, or Izzard et al. (2004) during the thermally-pulsing AGB. The initial radius of the post-AGB star is determined by the post-common envelope separation, which in turn depends on α_{CE} and λ_{CE} (Sec. 3.1). The post-(A)GB stellar radius and luminosity are calculated as in Hurley et al. (2000,

their Sec. 6.3). The binary has an eccentricity $e_{\text{post-CE}}$ just after the common envelope is ejected, with $e_{\text{post-CE}} = 10^{-5}$ by default. Hydrodynamic common-envelope models (e.g. Passy et al. 2012) predict eccentricities of about 0.1 but these simulations never conclude full envelope ejection, so the true value is probably less because of subsequent tidal damping.

In the absence of a circumbinary disc a post-(A)GB star loses material from its hydrogen-rich envelope in a stellar wind while hydrogen burning eats into it from below. We use the BINARY_C default mass-loss prescription, which is based on that of Hurley et al. (2002). On the AGB, the Vassiliadis & Wood (1993) rate dominates, but as the star transitions to the post-AGB the Nieuwenhuijzen & de Jager (1990) Wolf-Rayet rate takes over. This is typically a bit less than $10^{-7} M_{\odot} \text{ yr}^{-1}$ in our IRAS 08544-4431 simulations. We discuss other mass-loss prescriptions in Sec. 5.3. Nuclear burning also consumes the envelope at about $10^{-7} M_{\odot} \text{ yr}^{-1}$. As the hydrogen envelope thins the star heats, eventually becomes a white dwarf, and subsequently cools and dims.

When there is a circumbinary disc, mass flows from its inner edge onto the post-(A)GB star (Eq. 49), rejuvenating the hydrogen envelope and extending the post-(A)GB phase. If the post-(A)GB star expands and overflows its Roche lobe as a result of this accretion, we allow mass to transfer to its companion but do not repeat common-envelope evolution. This seems reasonable because the envelope, even though it is convective, has little enough mass to shrink in response to mass loss, but we admit a more realistic treatment of such phases is currently lacking (cf. Halabi et al. 2018).

3.5 Disc termination

Our evolution algorithm must be fast because we wish to evolve millions of binary stars in stellar population simulations. We thus choose conditions under which disc evolution is terminated to prevent excessive and unnecessary numerical computation of discs which would not be observed.

When the mass of the circumbinary disc falls below $M_{\text{min}} = 10^{-6} M_{\odot}$ or it dims below $L_{\text{min}} = 10^{-4} L_{\odot}$ we terminate its evolution. Such discs are difficult to observe and, because of their low mass, hardly affect subsequent binary evolution.

If the time-scale for disc evaporation by slow mass loss, $M_{\text{disc}}/\dot{M}_{\text{slow}}$ (Eq. 45), is shorter than 1 yr we evaporate the disc instantly, thus stopping its evolution. This happens when the X-ray induced wind becomes strong as the post-(A)GB star heats: typically the disc evaporates before $T_{\text{eff}} \approx 4 \times 10^4 \text{ K}$.

We also terminate disc evolution when,

$$f_{\text{Ring}} = \frac{R_{\text{out}}}{R_{\text{in}}} - 1 < 0.2. \quad (57)$$

Such discs are narrow rings with which our solution method sometimes struggles (Sec. 2.5), and observed post-AGB discs have $f_{\text{Ring}} \gg 1$ so are not such objects.

4 THE CIRCUMBINARY DISC AROUND IRAS 08544-4431

ALMA CO molecular-line maps of the circumbinary disc around IRAS 08544-4431 show it has a mass of about $0.02 M_{\odot}$ and surrounds a central binary with orbital period 508 d, eccentricity 0.22 and total mass $1.8 M_{\odot}$ containing a $0.65 M_{\odot}$, 7250 K, F3, $1.2 \times 10^4 L_{\odot}$ post-AGB star with $[\text{Fe}/\text{H}] = -0.5$ ($Z \approx 0.004$ assuming $Z_{\odot} = 0.014$) and a $1.15 M_{\odot}$ companion, assuming a distance

of 1100 pc (Bujarrabal et al. 2018; Kluska et al. 2018). The orbital separation is thus $a \approx 325 R_{\odot} \approx 1.5$ au.

The inner edge of the gas disc is not resolved but the inner edge of dust lies at 9 au (Deroo et al. 2007). The outer edge is at 4.0×10^{16} cm $\approx 5.7 \times 10^5 R_{\odot} \approx 2700$ au. The disc mass is $0.6 - 2.0 \times 10^{-2} M_{\odot}$. The disc angular momentum is about $13 M_{\odot} \text{ km s}^{-1} \text{ au} \approx 3.9 \times 10^{52} \text{ g cm}^2 \text{ s}^{-1}$ compared to the orbital angular momentum of about $20 M_{\odot} \text{ km s}^{-1} \text{ au} \approx 6.1 \times 10^{52} \text{ g cm}^2 \text{ s}^{-1}$. The cubic dependence of angular momentum on the assumed distance introduces considerable uncertainty, as discussed in detail by Bujarrabal et al. (2018), and, if a distance of 550 pc is assumed, the orbital angular momentum may be as small as $1.6 M_{\odot} \text{ km s}^{-1} \text{ au} = 4.8 \times 10^{51} \text{ g cm}^2 \text{ s}^{-1}$.

4.1 Progenitor binary system

The mass and luminosity of the post-AGB star, $0.65 M_{\odot}$ and $1.2 \times 10^4 L_{\odot}$ respectively, are too massive and too bright to support the idea that mass transfer started during the first ascent of the red giant branch. IRAS 08544-4431 is thus a true post-AGB system. If mass transfer starts on the early-AGB (EAGB), a star with a $0.65 M_{\odot}$ core has a total mass of $2.4 M_{\odot}$ and a radius of about $200 R_{\odot}$. This is shorter than the current orbital separation, $330 R_{\odot}$, so is impossible if we assume common-envelope evolution only shortens the separation. The star is thus likely a post-TPAGB star.

The TPAGB star had a core of mass $0.65 M_{\odot}$ when it lost its envelope, so with a metallicity $Z = 0.004$ must have had an initial mass of less than about $2.8 M_{\odot}$ (cf. Fig. 2 of Izzard et al. 2004 based on the models of Karakas et al. 2002). Its initial mass must exceed $1.2 M_{\odot}$ to become a giant before its companion evolves from the main sequence.

In Fig. 1 we show the initial $a - M_1$ parameter space that corresponds to a post-AGB system with $M_1 = 0.65 \pm 0.05 M_{\odot}$ and $a = 330 \pm 50 R_{\odot}$ with either $\alpha_{\text{CE}} = 1.0$ or 0.2 (De Marco et al. 2011; Davis et al. 2012). When $\alpha_{\text{CE}} = 0.2$, the energy available to eject the common envelope is so limited that wind mass loss must remove much of the stellar envelope before Roche-lobe overflow starts. Such systems typically eject a common envelope of mass 0.2 to $0.8 M_{\odot}$, so to make a $0.02 M_{\odot}$ disc requires $f_M = 0.025 - 0.10$. When $\alpha_{\text{CE}} = 1$ more energy is available to eject the common envelope so wind mass loss is not as important and the common envelope mass is $0.8 - 1.6 M_{\odot}$ corresponding to $f_M = 0.0125 - 0.025$. Without a good constraint on α_{CE} in AGB binaries we cannot say which of the above scenarios is more likely, only that in both we have sufficient mass to make the required circumbinary disc.

The angular momentum of the circumbinary disc around IRAS 08544-4431 is $0.48 - 6.1 \times 10^{52} \text{ g cm}^2 \text{ s}^{-1}$. Fig. 2 shows that there is sufficient angular momentum in the common envelope ejected from all our progenitor systems to make the disc. In both our above example systems, $J_{\text{orb}} \approx 1.7 \times 10^{53} \text{ g cm}^2 \text{ s}^{-1}$ so $2.8 - 36$ per cent of the orbital angular momentum goes into the circumbinary disc.

In the following, we set initial stellar masses $M_1 = 2.00 M_{\odot}$ and $M_2 = 1.15 M_{\odot}$, initial separation $a_{\text{init}} = 900 R_{\odot}$, metallicity $Z = 0.004$ and adopt $\alpha_{\text{CE}} = 1.0$. The post-AGB system thus has $M_1 = 0.64 M_{\odot}$, $M_2 = 1.16 M_{\odot}$, $L_1 \approx 0.95 \times 10^4 L_{\odot}$ and separation $a = 331 R_{\odot}$, which are similar to the properties of the binary at the centre of IRAS 08544-4431.

4.2 Initial disc structure model

To initially model the disc around IRAS 08544-4431 we set $f_M = 0.01$ and $f_j = 0.10$, along with $\Gamma = 1.4$, $\kappa = 0.01 \text{ cm}^2 \text{ g}^{-1}$, $f_{\text{tid}} =$

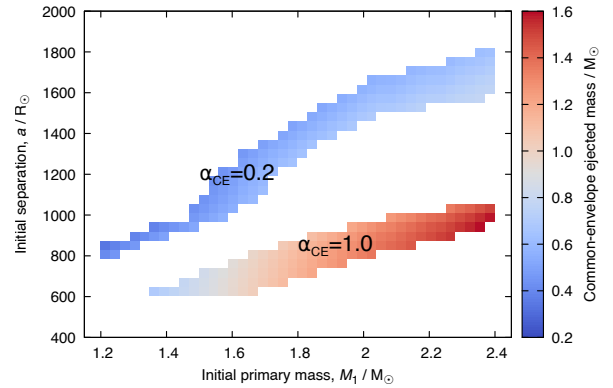


Figure 1. The initial separation and mass of systems which, with our common-envelope prescription using $\alpha_{\text{CE}} = 0.2$ and 1.0 and $f_{\text{ion}} = 0.1$, exit the common-envelope phase with a post-AGB primary of mass $M_1 = 0.65 \pm 0.05 M_{\odot}$ and orbital separation $a = 330 \pm 50 R_{\odot}$, assuming an initial secondary and post-common envelope mass $M_2 = 1.15 M_{\odot}$. The colour represents the mass of the ejected common envelope. These systems are possible progenitors of IRAS 08544-4431 assuming about 1 per cent of the common envelope mass forms a circumbinary disc.

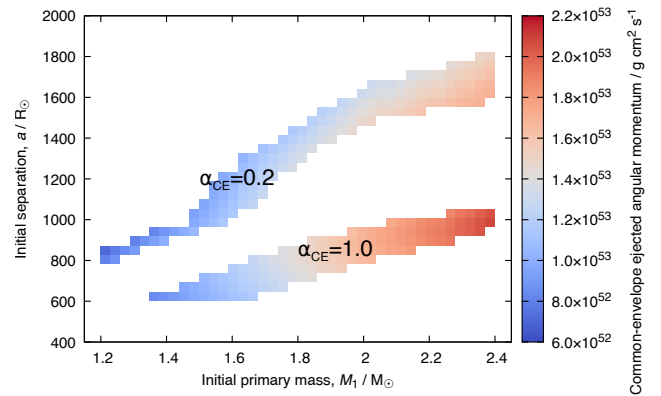


Figure 2. As Fig. 1 but showing angular momentum ejected during common-envelope evolution rather than mass.

10^{-3} and $\alpha_{\text{disc}} = 10^{-3}$ (model parameters are listed in table 3). This results in a disc of mass $0.013 M_{\odot}$ with $J_{\text{disc}} = 1.7 \times 10^{52} \text{ g cm}^2 \text{ s}^{-1} = 5.7 M_{\odot} \text{ km s}^{-1} \text{ au}$. In Fig. 3 we show how the initial properties of the disc vary as the above parameters are varied in turn. Observables correspond to the range of solutions found by Bujarrabal et al. (2018) and we assume that the present-day IRAS 08544-4431 differs little compared to its birth state (Sec. 4.3 justifies this).

A narrow disc-mass range, $0.005 \lesssim f_M \lesssim 0.015$, matches IRAS 08544-4431 (Fig. 3 aa). To form a stable disc, the angular momentum fraction $f_j \gtrsim 0.015$ such that $J_{\text{disc}} \gtrsim 2.5 \times 10^{51} \text{ g cm}^2 \text{ s}^{-1}$ (Fig. 3 bb). Smaller discs are rings that fail the condition of Eq. 57.

Of the remaining parameters, κ is irrelevant because the viscous zone (Eq. 17) lies inside the binary orbit so is not in the disc. The tidal parameter f_{tid} and disc viscosity parameter α_{disc} affect the inner edge conditions, R_{in} and T_{in} , which are not constrained by observations. The inner radius lies at approximately twice the orbital separation, $R_{\text{in}} \approx 700 R_{\odot} \approx 2a \approx 3.3$ au, when $f_{\text{tid}} = 10^{-3}$. When $f_{\text{tid}} \lesssim 10^{-4}$ part of the disc lies inside the binary orbit so is removed, reducing the mass of the disc. Deroo et al. (2007) find the inner edge of the dust to be at about 9 au, which is consistent with our model. Their disc model

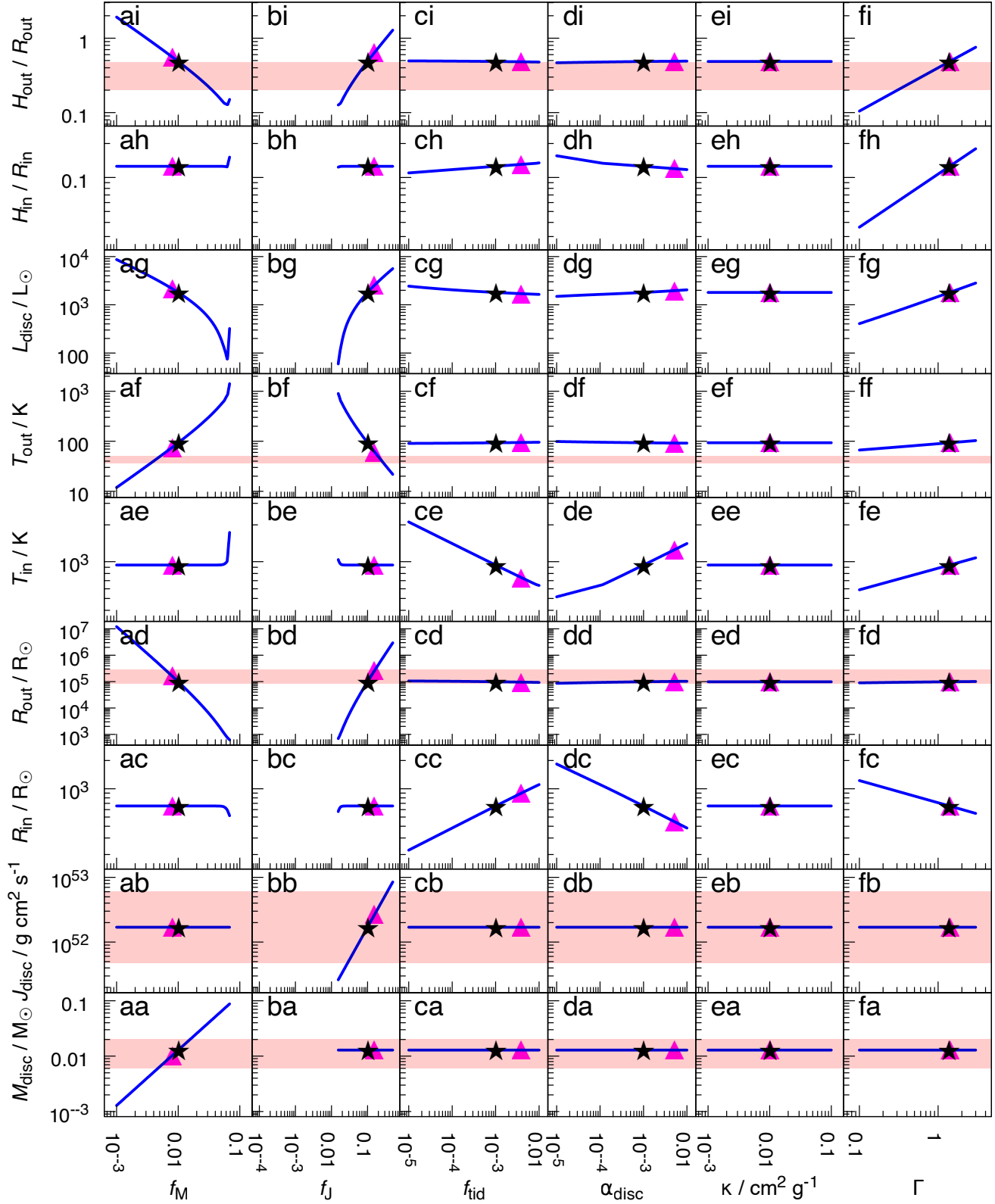


Figure 3. Sensitivity of observable properties of our circumbinary disc just after it forms, i.e. when the common-envelope is ejected, to the main parameters in our disc model. The blue lines show how the observable (ordinate) varies when each parameter (abscissa) is changed in turn with all other parameters set to their defaults (Table 3). The black stars are our initial guess for the parameters (Sec. 4.2) while the magenta triangles are our best-fitting model parameters (Sec. 4.4). The pink, shaded region represents the disc observed around IRAS 08544-4431 where the range is mostly because of its uncertain distance (Bujarrabal et al. 2018). f_M and f_J are the fraction of the common-envelope mass and angular momentum that are used to make the disc (Eqs. 1 and 2), f_{tid} multiplies the torque that acts on the disc (Eq. 53), α_{disc} is the disc viscosity parameter (Eq. 15), κ is the disc opacity (Eq. 4) and Γ is the adiabatic index (Eq. 13). M_{disc} is the disc mass, J_{disc} is the disc angular momentum, R_{in} and R_{out} are the inner and outer radii of the disc, respectively, T_{in} and T_{out} are the inner and outer edge temperatures of the disc, respectively, and $H_{\text{out}}/R_{\text{out}}$ and $H_{\text{in}}/R_{\text{in}}$ are the ratios of the disc scale height to its radius at its inner and outer edge, respectively.

Table 3. Parameters in our disc model, their default values as used in our initial guess for the structure of the disc around IRAS 08544-4431, the subsequent best fits to observed disc properties based on MCMC modelling (Sec. 4.4), and brief descriptions.

Parameter	Default	Best fit	Definition	Description
f_M	0.010	0.0079	Eq. 1	Fraction of the common envelope mass that is put into the circumbinary disc.
f_j	0.10	0.16	Eq. 2	Fraction of the common envelope angular momentum that is put into the circumbinary disc.
κ	$10^{-2} \text{ cm}^2 \text{ g}^{-1}$		Eq. 4	Opacity in the circumbinary disc.
Γ	1.4		Eq. 13	Adiabatic index in the circumbinary disc, used to define the speed of sound.
α_{disc}	10^{-3}	5.0×10^{-3}	Eq. 15	Disc viscosity parameter.
f_{visc}	1		Eq. 49	Multiplies the mass accretion rate from the inner edge of the circumbinary disc onto the binary stars.
$f_{\text{visc},J}$	0.6		Eq. 50	Multiplies the angular momentum accretion rate from the inner edge of the circumbinary disc onto the binary stars.
f_{tid}	10^{-3}	4.0×10^{-3}	Eq. 53	Multiplies the torque acting on the circumbinary disc.
f_{res}	1		Eq. 55	Multiplies the rate of eccentricity pumping of the binary star system.
f_X	1		Sec. 3.2.1	Multiplies the X-ray flux incident on the disc.
$e_{\text{post-CE}}$	10^{-5}		Sec. 3.4	Eccentricity of the binary just after common envelope ejection.

is in 2D with radiation transport, compared to our simpler but faster 1D model. Their 2D solutions include a puffed-up inner edge and shadowed region. Our disc inner-edge is always cooler than their 2D disc solution, $T_{\text{in}} \sim 800 - 900 \text{ K}$ in our 1D model compared to their assumed 1500 K inner edge at the dust condensation temperature. The difference in T_{in} between their model and ours, $\sim 600 \text{ K}$, far exceeds the $\sim 200 \text{ K}$ numerical uncertainties in our temperature solution. The differences most likely arise because we do not model the puffed-up edge which has $H_{\text{in}}/R_{\text{in}} = 0.22$ in their 2D model compared to our simplified 1D disc which has $H_{\text{in}}/R_{\text{in}} \sim 0.11$.

The initial outer edge properties, R_{out} , T_{out} and $H_{\text{out}}/R_{\text{out}}$, better match the observations if Γ is reduced below its default 1.4, but this is difficult to justify physically. Our assumption that the disc is Keplerian throughout, while IRAS 08544-4431 is not quite Keplerian near its outer edge, could be responsible. Our disc equations also assume $H/R \ll 1$ which is not strictly true (e.g. Corporaal et al. 2021). Increasing the angular momentum in our disc improves the match to R_{out} (Fig. 3 bd) but worsens the matches to the temperature T_{out} (Fig. 3 bf) and the ratio $H_{\text{out}}/R_{\text{out}}$ (Fig. 3 bi).

4.3 Disc Evolution

The evolution of temperature, density and total mass of our default model of IRAS 08544-4431 is shown in Fig. 4. Other than slow changes to its mass and angular momentum because of flow through its inner edge and torque from the inner binary, respectively, our disc is stable for most of its life. It loses mass through its inner edge at a rate around $2.5 \times 10^{-8} M_{\odot} \text{ yr}^{-1}$ (cf. Eq. 49). If this were the only source of mass loss, the disc would evaporate in about $4 \times 10^5 \text{ yr}$. Unfortunately for our disc, the post-AGB star’s hydrogen-burning shell eats through its hydrogen envelope more quickly, at a rate of about $10^{-7} M_{\odot} \text{ yr}^{-1}$, with a corresponding lifetime of about $3 \times 10^4 \text{ yr}$. As the envelope thins, the star heats and its X-ray flux increases. X-ray induced mass loss evaporates the disc after about $2.9 \times 10^4 \text{ yr}$. By this time the X-ray luminosity of the post-AGB star is around $0.01 L_{\odot}$ ($3 \times 10^{31} \text{ erg s}^{-1}$) which is sufficient to evaporate similar protoplanetary discs (cf. Monsch et al. 2019).

The final panel of Fig. 4 shows the binary eccentricity e versus disc age. Over its lifetime the disc pumps the binary eccentricity from $e = e_{\text{post-CE}} = 10^{-5}$ to nearly 0.1. The eccentricity of IRAS 08544-4431 is 0.22 ± 0.02 (Kluska et al. 2018). Increasing $e_{\text{post-CE}}$ does not solve this discrepancy. To reach $e = 0.22$ requires a post-common envelope eccentricity $e_{\text{post-CE}} = 0.19$, double that seen in hydrodynamical simulations of common-envelope evolution (e.g. Passy et al. 2012).

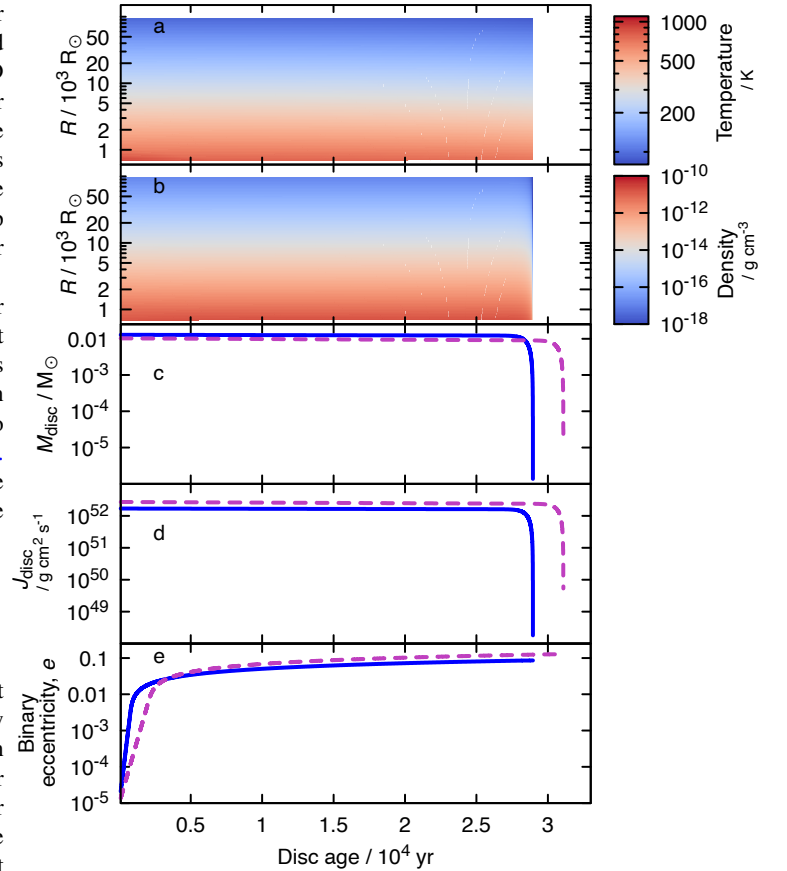


Figure 4. Disc temperature (a) and density (b) as a function of radius and time in our initial guess disc model, and disc mass (c), angular momentum (d) and binary eccentricity (e) as a function of time in our initial guess model (blue, solid lines) and best-fitting model (magenta, dashed lines) of IRAS 08544-4431. In both models, the disc hardly changes until the X-ray flux from the post-AGB star is sufficient to evaporate it at about $3 \times 10^4 \text{ yr}$.

A factor 2.8 increase to the rate of Eq. 55, with $e_{\text{post-CE}} = 10^{-5}$, is sufficient to reach $e = 0.22$.

Fig. 5 shows the time-averaged properties of the disc and its lifetime as a function of its input parameters. As described above, because the disc changes little over most of its lifetime, these properties are similar to the initial disc properties, with a lifetime just short of $3 \times 10^4 \text{ yr}$.

Massive discs, with $f_M \sim 0.03\text{--}0.05$ and $f_J = 0.1$, are exceptional. Because of their extra mass, the viscous inflow rate at the inner edge is similar to the burning rate of the hydrogen-burning shell of the post-AGB star, prolonging its life up to about 10^5 yr. These discs are relatively compact, with outer radii shorter than $10^4 R_\odot$, so do not look like IRAS 08544-4431 which has an outer radius in excess of $10^5 R_\odot$. However, if such discs are formed, their long lifetimes make them more likely to be observed and their stars' thick hydrogen envelopes keep their stars relatively cool (~ 3000 K). We caution the reader: the sweet spot in f_M that leads to long disc life corresponds to a particular choice of f_J and f_{visc} . Choosing an even greater $f_M = 0.06$ results in the disc being too compact to live very long – it quickly forms a compact ring and is evaporated after about 10^3 yr, while even more massive discs cannot form because they lack sufficient angular momentum. If, with $f_M = 0.06$, we also set $f_J = 0.2$ the disc lives for 1.8×10^5 yr. If f_{visc} is smaller than the default, 1, the mass of accreted hydrogen is reduced and the disc lives for less time as a result of the star reaching a temperature of $\sim 3 \times 10^4$ K more quickly, at which point the disc is evaporated. The exception to this is if the disc runs out of mass, but this does not happen in any of our models with $f_M > 10^{-4}$, $f_J = 0.1$ and $f_{\text{visc}} < 1$. These systems always evaporate their discs by X-ray-induced winds.

4.4 Best-fitting disc parameters

We now attempt to fit our disc parameters, f_M , f_J , f_{tid} and α_{disc} , to IRAS 08544-4431 using our initial model as a first guess. We match time-averaged disc properties from our model (Fig. 5) to observed M_{disc} , J_{disc} , R_{out} , T_{out} and $H_{\text{out}}/R_{\text{out}}$ (Bujarrabal et al. 2018). We assume that each observable takes the mean value of the extremes given by assuming distances of 550 and 1100 pc, we further assume the associated error is Gaussian with the 1σ error set to half the range of the observable. Thus $M_{\text{disc}} = 1.3 \pm 0.7 \times 10^{-2} M_\odot$, $J_{\text{disc}} = 3.29 \pm 2.81 \times 10^{52} \text{ g cm}^2 \text{ s}^{-1}$, $R_{\text{out}} = 1.3 \pm 0.7 \times 10^{16} \text{ cm}$, $T_{\text{out}} = 43 \pm 7 \text{ K}$ and $H_{\text{out}}/R_{\text{out}} = 0.33 \pm 0.13$. We further can assume $\dot{M}_{\text{visc}} = 10^{-7} \pm 0.5 \times 10^{-7} M_\odot \text{ yr}^{-1}$ and $R_{\text{in}}/a = 2.00 \pm 0.25$ as in previous works on circumbinary discs (e.g. Dermine et al. 2013). We employ EMCEE (Foreman-Mackey et al. 2019) to perform a Markov-Chain Monte Carlo exploration of the parameter space using 46 walkers with chain lengths of 2000, each of which has its first 100 samples discarded. We assume flat priors in the ranges $-7 < \log_{10} \alpha < 0$, $-5 < \log_{10} f_{\text{tid}} < -1$, $-4 < \log_{10} f_M < -1$ and $-4 < \log_{10} f_J < 0$.

The resulting best-fit parameters are $\log_{10} \alpha_{\text{disc}} = -2.3_{-0.6}^{+1.4}$, $\log_{10} f_{\text{tid}} = -2.4_{-0.6}^{+1.4}$, $\log_{10} f_M = -2.1_{-0.3}^{+0.7}$ and $\log_{10} f_J = -0.8_{-0.2}^{+0.6}$, where the values quoted are the means of the resulting distributions and uncertainties are 1σ (Fig. D1). Without constraints on \dot{M}_{visc} and R_{in}/a we cannot well constrain α_{disc} or f_{tid} (Fig. D2) but find similar f_M and f_J : $\log_{10} f_M = -2.2_{-0.3}^{+1.2}$ and $\log_{10} f_J = -0.8_{-0.3}^{+0.7}$.

4.5 Sensitivity to evolutionary parameters

In this section we examine how our disc model reacts to reasonable changes in its input parameters: α_{disc} , Γ , κ , f_X , $f_{\text{visc},J}$, f_{visc} , f_{res} , f_{tid} , f_J and f_M . We use a Levenburg-Marquhart algorithm (Press et al. 1992) to fit functions of the form,

$$\log_{10}(y) = \Phi + \Upsilon \log_{10}(x/x_0) + \Theta [\log_{10}(x/x_0)]^2, \quad (58)$$

where y is a property of the disc that depends on parameter x and x_0 is our default value of the parameter. Φ , Υ and Θ are the constant parameters of each fit. We fit the time-averaged inflow rate at the inner edge, \dot{M}_{visc} , luminosity, $\overline{L_{\text{disc}}}$, inner and outer radii, $\overline{R_{\text{in}}}$ and $\overline{R_{\text{out}}}$

respectively, scale height ratios at the inner and outer edge, $\overline{H_{\text{in}}/R_{\text{in}}}$ and $\overline{H_{\text{out}}/R_{\text{out}}}$ respectively, and the mean binary-star eccentricity, \overline{e} . We also fit the maximum eccentricity of the binary system, e_{max} , the minimum Toomre parameter, Q_{min} , and the disc lifetime, t_{disc} . Appendix C shows the resulting fitting functions and lists the coefficients. In the following, we consider each observable property of the disc, mostly in the form of power laws, $y \approx y_0 x_0^k$, around our default model.

Disc lifetime depends mostly on the mass in the disc. This is set by f_M which governs the initial disc mass. Making the disc more compact by reducing f_J has a similar effect to increasing f_M . Secondly, mass loss from the inner edge of the disc, regulated through the viscosity parameter α_{disc} and multiplier f_{visc} , is also important. Together, the disc lifetime scales as $2.9 \times 10^4 (\alpha_{\text{disc}}/0.001)^{0.13} (f_{\text{visc}})^{0.12} (f_J/0.1)^{-0.21} (f_M/0.01)^{0.51}$ yr. The X-ray wind multiplier, f_X , has a relatively small impact on lifetime, as long as f_X is non-zero, because the post-AGB X-ray flux increases extremely quickly as the star contracts and heats.

Disc size The inner radius, R_{in} , is a strong function of the tidal torque on the disc, through f_{tid} , and the gas properties α_{disc} and Γ , such that $\overline{R_{\text{in}}} \approx 674 (\alpha_{\text{disc}}/0.001)^{-0.21} (\Gamma/1.4)^{-0.24} (f_{\text{tid}}/0.001)^{0.22} R_\odot$.

The outer radius depends primarily on the disc specific angular momentum through f_J and f_M , with $\overline{R_{\text{out}}} \approx 1.0 \times 10^5 (f_J/0.1)^{2.3} (f_M/0.01)^{-2.2} R_\odot$.

Disc luminosity is a function of disc size hence specific angular momentum and Γ , such that $\overline{L_{\text{disc}}} \approx 1640 (\Gamma/1.4)^{0.6} (f_J/0.1)^{0.99} (f_M/0.01)^{-0.88} L_\odot$.

Binary eccentricity is pumped to about $e = 0.1$ if R_{in} is inside the 2:1 Lindblad resonance, otherwise is less than 0.01. The parameters that change R_{in} are described above. We discuss eccentricity further in Sec. 5.

Disc scale height ratios are particularly sensitive to Γ , and the outer edge ratio also depends sensitively on the disc specific angular momentum, such that $\overline{H_{\text{in}}/R_{\text{in}}} \approx 0.117 (\Gamma/1.4)^{0.49}$ and $\overline{H_{\text{out}}/R_{\text{out}}} \approx 0.483 (\Gamma/1.4)^{0.58} (f_J/0.1)^{0.65} (f_M/0.01)^{-0.64}$.

Toomre's Q is defined such that $Q < 1$ implies gravitational instability and possible planet formation (Toomre 1964). We measure Q_{min} , the minimum Q at any point in the disc throughout its lifetime, and find this is sensitive to disc mass and specific angular momentum, as well as Γ , such that $Q_{\text{min}} \approx 284 (\Gamma/1.4)^{0.61} (f_J/0.1)^{0.92} (f_M/0.01)^{-1.9}$. All our simulated discs have $Q_{\text{min}} \gg 1$, so are not expected to form planets by gravitational collapse, contradicting the assumption of Schleicher & Dreizler (2014).

5 DISCUSSION

Our disc model allows us to evolve many discs in a stellar population efficiently yet still reasonably well models the circumbinary disc around IRAS 08544-4431. Below, we discuss some limitations, and strengths, of our model.

5.1 Model limitations

Our disc models assume constant opacity with a default $\kappa = 0.01 \text{ cm}^2 \text{ g}^{-1}$ originating from gas with no dust contribution. Opacity is only important when energy transport is dominated by viscous heating (Eq. 4), but in our disc around IRAS 08544-4431 this is never the case with $\kappa = 0.01 \text{ cm}^2 \text{ g}^{-1}$. If we set $\kappa = 10^5 \text{ cm}^2 \text{ g}^{-1}$ to force

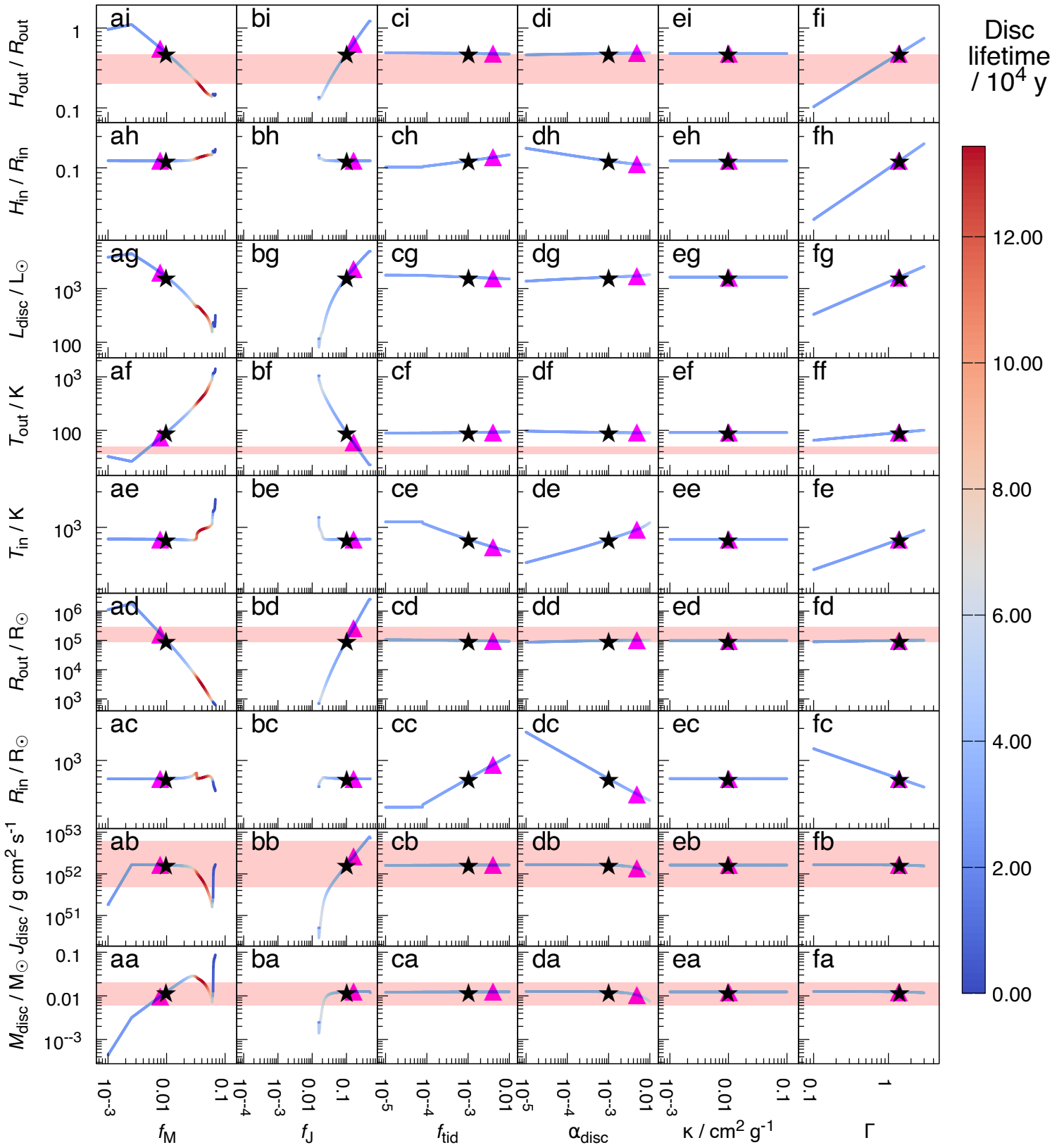


Figure 5. As Fig. 3 but instead showing time-averaged properties of the our disc model. The line colour represents the lifetime of the disc. The black star is our initial guess for the parameters (Sec. 4.2) while the magenta triangle is our best-fitting model (Sec. 4.4). Most discs live for about 4×10^4 yr because this is the time it takes the post-AGB star to heat sufficiently that the X-ray-induced disc-wind evaporates the disc. More massive discs, with $f_M \sim 0.02 - 0.05$ have extended lifetimes because they can transfer more material onto the post-AGB star and keep it cool for longer (as discussed in Sec. 4.3). Discs can live for longer than shown here, $\geq 1.2 \times 10^5$ yr, but only if they lose little or no mass which our default parameter choices, designed to match observed circumbinary discs, do not allow. The other parameters shown here change the disc lifetime very little.

the entire disc to be one viscosity-dominated zone, our disc inner radius decreases from ~ 650 to $\sim 550 R_{\odot}$ and its luminosity increases from $1700 L_{\odot}$ to about $5000 L_{\odot}$. Other global properties such as the disc lifetime and its impact on the inner binary, e.g. through mass accretion and eccentricity pumping, change little. A two-zone model containing an inner gas-dominated and outer dust-dominated structure is beyond the scope of our model, but based on the lack of significant changes to the binary interaction our model seems reasonable if the goal is to investigate feedback on the stars and their orbit.

We also assume, for simplicity, that our disc is circular and aligned with the binary orbit. In our model, binaries eject their common envelopes with nearly-circular orbits – we assume $e_{\text{post-CE}} = 10^{-5}$ – and we perhaps naively neglect disc eccentricity. [Pichardo et al. \(2008\)](#) suggest that discs should be roughly circular even in moderately eccentric binaries, while [Muñoz & Lithwick \(2020\)](#) show that discs become eccentric even if the binary is circular because of eccentric mode trapping, and .

Many works, e.g. [Lubow et al. \(2015\)](#), [Miranda & Lai \(2015\)](#), [Nixon & Lubow \(2015\)](#) and [Franchini et al. \(2019\)](#), show that misinclination effects are complicated and highly non-linear, particularly if a third star is present ([Martin et al. 2022](#)). Merging the results of such simulations into our model is beyond its scope at present, but is certainly worth future investigation.

Our disc viscosity, modelled through α_{disc} , is assumed constant throughout the disc, but in reality depends on ionization fraction and hence the temperature distribution in the disc. Many features of the disc are sensitive to α_{disc} . Relevant to the inner binary evolution is the increased efficiency of eccentricity pumping, and mass and angular momentum transfer from the inner edge to the stars. The central binary in our default model with $\alpha_{\text{disc}} = 10^{-3}$ suffers net loss of angular momentum from the binary to the disc because mass is accreted at about $2 \times 10^{-8} M_{\odot} \text{ yr}^{-1}$ which is insufficient to balance the torque imparted on the disc. With $\alpha_{\text{disc}} = 10^{-2}$ the situation is reversed and the inner binary gains angular momentum by accretion of mass at a rate of $1 - 3 \times 10^{-7} M_{\odot} \text{ yr}^{-1}$. The accreted material keeps the central post-AGB star cool, thus limiting the wind from the disc and doubling its age to nearly $6 \times 10^4 \text{ yr}$ (Sec. finalfates). While we can, in theory, use the mass accretion rate in a comparison with observations to constrain α_{disc} , as in Fig. D1, other observable disc properties such as the outer radius or outer temperature are not greatly affected by a change in α_{disc} . The post-AGB lifetime is also affected by accretion, so number counts of post-AGB binaries could also constrain α_{disc} but, given the many biases and uncertainties in calculating such quantities, e.g. assumed star-formation histories and selection functions, this will be a significant challenge. a

Our disc energy balance equation assumes all energy impacting the disc is absorbed and re-emitted, but perhaps we should assume a more realistic albedo. For an albedo ψ we can simply scale the incoming stellar flux, F_{\star} , by $1 - \psi$. The effect on disc properties is small because $L \sim T^4$ hence $\delta T/T \sim \delta L/(4L)$. Albedo is measured to be $\sim 30\%$ in the R band in 89 Her, seen pole on ([Hillen et al. 2014](#)). With an albedo of 0.5 applied to our model of IRAS 08544-4431 the lifetime is reduced by only 500 yr and the eccentricity reaches 0.073 compared to 0.087. Both are negligible changes.

The work of [Corporaal et al. \(2021\)](#) confirms that IRAS 08544-4431 has a puffed-up inner edge, which is not taken into account in our model and probably accounts for our (gas) inner edge temperature, about 1000 K, being cooler than the observed H -band temperature of $1290 \pm 70 \text{ K}$ (this difference is small enough to be swallowed by our model uncertainty, Sec. 2.3). They also found that $T \propto r^{-0.8}$. Our best-fitting model of IRAS 08544-4431 starts

with two zones, with exponents $-3/7 \approx -0.43$ and $-3/4$, then at about 7000 yr has one zone with exponent $-3/4$. This latter solution agrees well with the observed temperature gradient.

[Bailer-Jones et al. \(2021\)](#) recently estimated the distance estimate of IRAS 08544-4431 to $1.53 \pm 0.12 \text{ kpc}$ which, combined with the inner-edge radius estimate of [Corporaal et al. \(2021\)](#) gives $R_{\text{in}} \approx 2000 R_{\odot}$. This is outside our gas-disc inner edge, at around $600 R_{\odot}$ in our best betting model, although our dust disc temperature at $2000 R_{\odot}$ is still only 765K, presumably because our model lacks the inner dust ring modelled in [Corporaal et al. \(2021\)](#).

5.2 The origin of circumbinary-disc systems

We assume the disc around IRAS 08544-4431 is made by the ejection of a common-envelope but the disc could form from stellar winds ([Kervella et al. 2016](#)) if they start in a wide binary that shrinks to the present orbit (e.g. [Izzard et al. 2010](#)), or a binary that has stable mass transfer, perhaps with L_2 mass loss. This does not affect our results except from a binary evolutionary point of view. Similar systems to IRAS 08544-4431 have a large eccentricity, often $e > 0.6$ ([Oomen et al. 2018](#)), favouring the wind mass transfer hypothesis as tides are expected to be very efficient in stars close to, or overflowing, their Roche lobes. Unfortunately, wind mass transfer, often thought to perhaps be the origin of the eccentricity, seems not be able to overcome the circularization effect of tides either ([Saladino & Pols 2019](#)).

We use the fits to thin-envelope radius and luminosity, hence effective temperatures, of [Hurley et al. \(2002\)](#). [Miller Bertolami \(2016\)](#) and [Oomen et al. \(2020\)](#) show that the thermal pulse cycle, neglected in our model which assumes an average luminosity of the post-AGB star, is important in determining both the radius and luminosity. Given that our modelled post-AGB star is of low mass, it has a long thermal pulse cycle ($\gtrsim 10^4 \text{ yr}$) so is unlikely to have undergone more than a few thermal pulses while surrounded by a circumbinary disc. However, in the future this is something that should be taken into account in our models.

Finally, the question of whether IRAS 08544-4431 forms a planetary nebula, or ever had one, is an interesting one given that planetary nebulae typically have short-period central binaries ([Boffin & Jones 2019](#); [Jacoby et al. 2021](#)). Our circumbinary disc lives for about 30,000 yr, and its central star is only hot enough, $T_{\text{eff}} \gtrsim 3 \times 10^4 \text{ K}$, to ionise a planetary nebula in the last 5000 yr before the disc is evaporated. Given a typical dynamical lifetime of a planetary nebula in the LMC is about $3.5 \times 10^4 \text{ yr}$, it is difficult to rule out formation through the binary channel with a central object with a period as long as the 500 d of IRAS 08544-4431. The disc mass remaining when the nebula forms is near to its initial $0.01 M_{\odot}$ but this drops quickly as the central star heats up, so it seems unlikely that a system will concurrently host a planetary nebula and a circumbinary disc. The lifetime of such planetary nebulae should also be shorter than in equivalent-mass single stars, because the nebula will have been expanding for most of the $2.5 \times 10^4 \text{ yr}$ the disc has kept the its post-AGB star cool by accretion.

5.3 Final fate, stellar winds and planetary survival

Our post-common envelope, post-AGB star has a thin hydrogen envelope of mass $0.01 M_{\odot}$. This is eaten from below at about $1.3 \times 10^{-7} M_{\odot} \text{ yr}^{-1}$ by the hydrogen-burning shell that powers the stellar luminosity and from above by stellar winds. In our standard wind model, based on [Hurley et al. \(2002\)](#), the wind of [Nieuwen-](#)

huijzen & de Jager (1990) applies when the stellar luminosity exceeds $4 \times 10^3 L_{\odot}$ as in our IRAS 08544-4431 models which have $L_* = 7 - 9 \times 10^3 L_{\odot}$. This dominates the loss of the stellar envelope, as shown in Fig. 6a, and is the main reason the post-AGB lifetime is limited to about 3×10^4 yr. As an alternative, we implemented the recently-determined rate of (Krtićka et al. 2020, our Fig. 6b). This new rate is slow enough that it has little impact on the disc lifetime which extends to about 4.8×10^4 yr, similar to the 5.3×10^4 yr lifetime with no post-AGB mass loss (Fig. 6c). Also, with the Krtićka et al. (2020) rate the system reaches an eccentricity $e = 0.27$ which is closer to that observed, $e = 0.22$, in IRAS 08544-4431 than our default model.

The disc lifetime can be further extended by increasing the rate of mass inflow from the inner edge which then replenishes the post-AGB envelope, keeping the star cool and thus preventing disc evaporation (Fig. 7). Using the Krtićka et al. (2020) wind rate with $f_{\text{visc}} = 10$ (Eq. 49) indeed lengthens the life of the disc to about 8×10^4 yr. This is, however, not good for eccentricity pumping. The accretion onto the post-AGB star is so fast its envelope expands to fill its Roche lobe again, and in such circumstances tides prevent further eccentricity pumping which is limited to $e = 0.16$ (cf. Oomen et al. 2020). Our treatment of Roche-lobe overflow assumes a circular binary so may be considered dubious in cases like this, but the amount of mass transferred is very small because the post-AGB envelope mass contains $\lesssim 0.01 M_{\odot}$. Similar skepticism probably should be applied to our tidal formalism when the dissipating envelope is of such low mass.

Our use of a relatively simple X-ray induced wind prescription, designed for circumbinary discs around young-stellar objects, certainly could be criticised. However, the general form of such a wind – in that it evaporates the disc as the star heats up – is hard to deny. Once the disc mass is low enough, and accretion onto the central star is slower than the rate of hydrogen burning, the central star warms rapidly and mass loss is very quick (a few hundred years). Increasing or decreasing the X-ray wind rate by an order of magnitude makes negligible difference to the circumbinary disc lifetime for this reason.

The question of second-generation planet formation in binary systems is naturally fascinating, but with only around a dozen circumbinary planets observed such planets are apparently rare. A fraction ~ 10 per cent of post-AGB circumbinary discs may show signatures of such interactions because they lack infrared excess (Kluska et al. 2022). Our model of IRAS 08544-4431 has a Toomre Q of about 600, suggesting the disc is unlikely to suffer gravitational collapse and subsequent planet formation. Planets around the original binary could, if they survive common-envelope evolution, accrete material from and carve gaps in the circumbinary disc, and perhaps explain the transition discs observed by Kluska et al. (2022).

Nonetheless, if an Earth-mass planet is at $1.1 a_{\text{min}}$ when the binary is born, where $a_{\text{min}} \approx 2700 R_{\odot}$ is the minimum stable radius around our IRAS 08544-4431 binary (Mardling & Aarseth 2001), its orbit expands to about $4700 R_{\odot}$ after common envelope ejection. It is thus in the circumbinary disc, near the inner edge, where accretion is possible and the disc is densest. Furthermore, the disc is cool enough, $T \sim 500\text{K}$ at this radius, even in the Corporaal et al. (2021) model, to form dust grains and so perhaps accretion of these can continue even after the gas disc evaporates. Whether this process is efficient enough to be important is left to future work.

5.4 Code performance

Using BINARY_C to model the binary system of IRAS 08544-4431 to the end of the post-AGB phase takes, without disc evolution, about

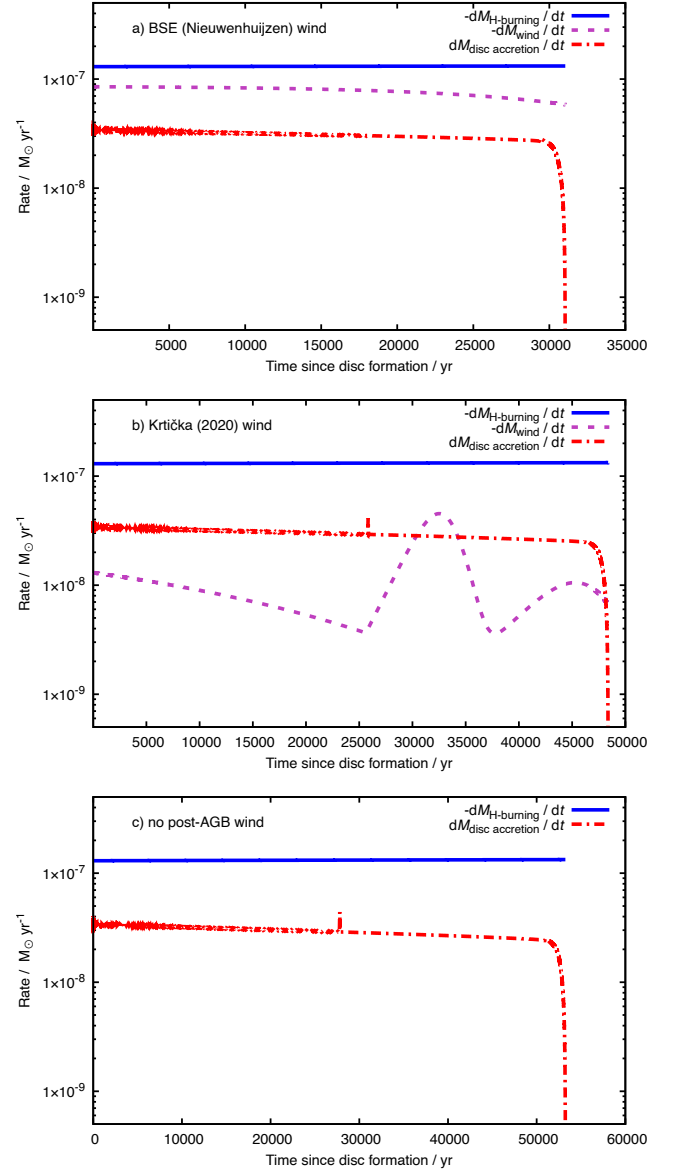


Figure 6. Comparison of the rate of post-AGB envelope destruction by hydrogen burning and wind mass loss, dM_{burning}/dt and dM_{wind}/dt , and replenishment by accretion from the inner edge of the circumbinary disc, $dM_{\text{disc accretion}}/dt$, in our best-fitting model of IRAS 08544-4431. Panel (a) shows our default model that uses the Hurley et al. (2002) wind prescription in which the Wolf-Rayet wind of Nieuwenhuijzen & de Jager (1990) dominates during the post-AGB phase, leading to disc evaporation after about 3×10^4 yr. Panel (b) uses the Krtićka et al. (2020) rate as an alternative which lengthens the post-AGB lifetime to about 5×10^4 yr because the post-AGB star remains relatively cool for longer. Panel (c) has no post-AGB wind loss and is similar to (b).

0.5 s on an Intel i7-1185G7 3.0 GHz CPU. Adding a circumbinary disc increases the run time to about 5.5 s. When simulating a population of binaries, only about 10 per cent are expected to form circumbinary discs from common-envelope evolution, so the run time of a binary-population approximately doubles when circumbinary discs are included. The estimate of 10 per cent represents the fraction of binaries that are born in the appropriate period range that mass transfer occurs on the upper first-giant branch or AGB such that the common envelope is ejected rather than the stars merge. Assuming

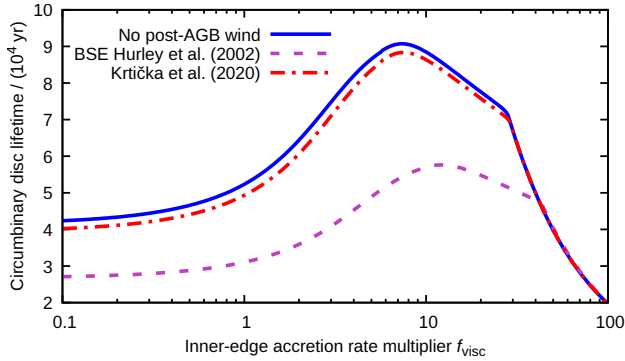


Figure 7. Circumbinary-disc lifetimes in our post-AGB models of IRAS 08544-4431 with no post-AGB wind (blue, solid line), the BSE wind of Hurley et al. (2002, red, dashed line) and the wind of Krtićka et al. (2020, magenta, dot-dashed line), as a function of the viscous inner-edge accretion multiplier, f_{visc} . At $f_{\text{visc}} = 0$ the lifetimes are equal to the post-AGB lifetime until $T_{\text{eff}} \approx 6 \times 10^4$ K. If inner-edge accretion is 5 to 10 times faster than the local viscous rate at the inner edge of the disc, the post-AGB lifetime more than doubles. At faster accretion rates, the finite amount of mass in the disc limits its lifetime. Systems with $f_{\text{visc}} \geq 5$ have fast enough accretion that the post-AGB star resumes Roche-lobe overflow.

$M_1 = 1M_{\odot}$, $M_2 = 0.5M_{\odot}$ and $\alpha_{\text{CE}} = 1$ and other physics as described as in Sec. 3.1, these systems have periods $\log_{10}(P/d) \sim 2-3$, i.e. ~ 1 dex. We usually model binary-star grids as a function of $0 \leq \log_{10} P \leq 8$, so this is about 12.5 per cent of these stars. Reducing α_{CE} to, say, 0.2, changes the range to $\log_{10}(P/d) \sim 2.4-3$ or about 7.5 per cent.

6 CONCLUSIONS

We present a fast evolutionary model of the circumbinary-disc system IRAS 08544-4431. The properties of our modelled disc, such as its mass and angular momentum, its outer radius, scale height and temperature, and mass accretion rate on the inner binary, agree reasonably well with observations. Our modelled inner edge radius is consistent with observations. In about 3×10^4 yr our circumbinary disc pumps the eccentricity of its inner binary to about 0.1 when $\alpha_{\text{disc}} = 10^{-3}$, half that observed in IRAS 08544-4431. A modest increase in α_{disc} allows us to match both the eccentricity in IRAS 08544-4431 and a viscous-timescale dominated accretion rate of $10^{-7} M_{\odot} \text{yr}^{-1}$, similar to that observed. Accretion onto the binary from the inner edge of the disc increases the duration of the post-AGB phase by only about 16 per cent compared to an equivalent single star. This lifetime is, instead, dominated by nuclear burning through its hydrogen envelope and stellar wind mass loss. Increasing the rate of inner edge accretion by a factor ~ 10 approximately doubles the lifetime of the post-AGB–circumbinary-disc system. We discuss both limitations and strengths of our model, the greatest of which is its speed. From birth to evaporation, our circumbinary-disc model takes about 5 s of computation time, making it suitable for binary-star population synthesis.

ACKNOWLEDGEMENTS

We thank the anonymous referee for their helpful comments. RGI thanks the STFC for funding his Rutherford fellowship under grant

ST/L003910/1, helping him through the difficult Covid-19 period with grant ST/R000603/1, Churchill College, Cambridge for his fellowship and access to their library. The Flatiron Institute is supported by the Simons Foundation. ASJ thanks the Gordon and Betty Moore Foundation (Grant GBMF7392), the National Science Foundation (Grant No. NSF PHY-1748958) and the UK Marshall Commission for supporting this work. This research has made use of NASA’s Astrophysics Data System Bibliographic Services. We thank Dave Green for his Cubehelix colour scheme (Green 2011). Many thanks go to, in no particular order and for useful discussions and help with this project, to Hans Van Winckel, Clio Gielen, Jacques Kluska, Glenn-Michael Oomen, Leen Decin, James Owen, Cathie Clarke, Richard Booth, Chris Tout, Philipp Podsiadlowski, Jason Isaacs and Hagai Perets.

DATA AVAILABILITY

The `BINARY_C` code developed for this project is available at its website, http://personal.ph.surrey.ac.uk/~ri0005/binary_c.html, and its Gitlab pages https://gitlab.eps.surrey.ac.uk/ri0005/binary_c and https://gitlab.com/binary_c. Data used and shown in this paper is available on reasonable request to the lead author.

References

- Armitage P. J., Natarajan P., 2002, *ApJ*, **567**, L9
- Bailer-Jones C. A. L., Rybizki J., Fousneau M., Demleitner M., Andrae R., 2021, *AJ*, **161**, 147
- Bocquet S., Carter F. W., 2016, *The Journal of Open Source Software*, 1
- Boffin H. M. J., Jones D., 2019, The Importance of Binaries in the Formation and Evolution of Planetary Nebulae, doi:10.1007/978-3-030-25059-1.
- Bujarrabal V., Alcolea J., Van Winckel H., Santander-García M., Castro-Carrizo A., 2013, *A&A*, **557**, A104
- Bujarrabal V., Castro-Carrizo A., Winckel H. V., Alcolea J., Contreras C. S., Santander-García M., Hillen M., 2018, *A&A*, **614**, A58
- Chachan Y., Booth R. A., Triaud A. H. M. J., Clarke C., 2019, *MNRAS*, **489**, 3896
- Chen W.-C., Podsiadlowski P., 2019, *ApJ*, **876**, L11
- Corporaal A., Kluska J., Van Winckel H., Bollen D., Kamath D., Min M., 2021, *A&A*, **650**, L13
- Cox D. P., 2005, *ARA&A*, **43**, 337
- Davis P. J., Kolb U., Knigge C., 2012, *MNRAS*, **419**, 287
- De Marco O., Izzard R. G., 2017, *Publ. Astron. Soc. Australia*, **34**, e001
- De Marco O., Passy J.-C., Moe M., Herwig F., Mac Low M.-M., Paxton B., 2011, *MNRAS*, **411**, 2277
- Dermine T., Izzard R. G., Jorissen A., Van Winckel H., 2013, *A&A*, **551**, A50
- Deroo P., Acke B., Verhoelst T., Dominik C., Tatulli E., van Winckel H., 2007, *A&A*, **474**, L45
- Dewi J. D. M., Tauris T. M., 2000, *A&A*, **360**, 1043
- Fleming D. P., Quinn T. R., 2017, *MNRAS*, **464**, 3343
- Foreman-Mackey D., et al., 2019, *The Journal of Open Source Software*, **4**, 1864
- Franchini A., Lubov S. H., Martin R. G., 2019, *ApJ*, **880**, L18
- Gallardo Cava I., Gómez-Garrido M., Bujarrabal V., Castro-Carrizo A., Alcolea J., Van Winckel H., 2021, *A&A*, **648**, A93
- Gerosa D., Veronesi B., Lodato G., Rosotti G., 2015, *MNRAS*, **451**, 3941
- Getley A. K., Carter B., King R., O’Toole S., 2017, *MNRAS*, **468**, 2932
- Green D. A., 2011, *Bulletin of the Astronomical Society of India*, **39**, 289
- Haiman Z., Kocsis B., Menou K., 2009, *ApJ*, **700**, 1952
- Halabi G. M., Izzard R. G., Tout C. A., 2018, *MNRAS*, **480**, 5176
- Haworth T. J., Booth R. A., Homan W., Decin L., Clarke C. J., Mohanty S., 2018, *MNRAS*, **473**, 317

- Hillen M., et al., 2014, *A&A*, **568**, A12
- Hurley J. R., Pols O. R., Tout C. A., 2000, *MNRAS*, **315**, 543
- Hurley J. R., Tout C. A., Pols O. R., 2002, *MNRAS*, **329**, 897
- Ivanova N., et al., 2013, *A&ARv*, **21**, 59
- Izzard R. G., Halabi G. M., 2018, arXiv e-prints, p. [arXiv:1808.06883](https://arxiv.org/abs/1808.06883)
- Izzard R. G., Tout C. A., Karakas A. I., Pols O. R., 2004, *MNRAS*, **350**, 407
- Izzard R. G., Dray L. M., Karakas A. I., Lugaro M., Tout C. A., 2006, *A&A*, **460**, 565
- Izzard R. G., Glebbeek E., Stancliffe R. J., Pols O. R., 2009, *A&A*, **508**, 1359
- Izzard R. G., Dermine T., Church R. P., 2010, *A&A*, **523**, A10
- Izzard R. G., Hall P. D., Tauris T. M., Tout C. A., 2012, in *Proceedings of IAU Symposium 283*. pp 95–102, doi:[10.1017/S1743921312010769](https://doi.org/10.1017/S1743921312010769)
- Izzard R. G., Preece H., Jofre P., Halabi G. M., Masseron T., Tout C. A., 2018, *MNRAS*, **473**, 2984
- Jacoby G. H., et al., 2021, *MNRAS*, **506**, 5223
- Karakas A. I., Lattanzio J. C., Pols O. R., 2002, *Publ. Astron. Soc. Australia*, **19**, 515
- Kashi A., Soker N., 2011, *MNRAS*, **417**, 1466
- Kervella P., Homan W., Richards A. M. S., Decin L., McDonald I., Montargès M., Ohnaka K., 2016, *A&A*, **596**, A92
- King A., 1998, *Monthly Notices of the Royal Astronomical Society*, **296**, L45
- Kley W., Haghighipour N., 2015, *A&A*, **581**, A20
- Kluska J., Hillen M., Van Winckel H., Manick R., Min M., Regibo S., Royer P., 2018, *A&A*, **616**, A153
- Kluska J., Van Winckel H., Coppée Q., Oomen G. M., Dsilva K., Kamath D., Bujarrabal V., Min M., 2022, *A&A*, **658**, A36
- Krtička J., Kubát J., Krtičková I., 2020, *A&A*, **635**, A173
- Lubow S. H., Martin R. G., Nixon C., 2015, *ApJ*, **800**, 96
- Lynden-Bell D., Pringle J. E., 1974, *MNRAS*, **168**, 603
- Mardling R. A., Aarseth S. J., 2001, *MNRAS*, **321**, 398
- Martin R. G., Lepp S., Lubow S. H., Kenworthy M. A., Kennedy G. M., Vallet D., 2022, *ApJ*, **927**, L26
- Miller Bertolami M. M., 2016, *A&A*, **588**, A25
- Miranda R., Lai D., 2015, *Monthly Notices of the Royal Astronomical Society*, **452**, 2396
- Monsch K., Ercolano B., Picogna G., Preibisch T., Rau M. M., 2019, *MNRAS*, **483**, 3448
- Muñoz D. J., Lithwick Y., 2020, *ApJ*, **905**, 106
- Muñoz D. J., Miranda R., Lai D., 2019, *ApJ*, **871**, 84
- Muñoz D. J., Lai D., Kratter K., Miranda R., 2020, *ApJ*, **889**, 114
- Nieuwenhuijzen H., de Jager C., 1990, *A&A*, **231**, 134
- Nixon C., Lubow S. H., 2015, *MNRAS*, **448**, 3472
- Oomen G.-M., Van Winckel H., Pols O., Nelemans G., Escorza A., Manick R., Kamath D., Waelkens C., 2018, *A&A*, **620**, A85
- Oomen G.-M., Pols O., Van Winckel H., Nelemans G., 2020, *A&A*, **642**, A234
- Owen J. E., Clarke C. J., Ercolano B., 2012, *MNRAS*, **422**, 1880
- Passy J.-C., et al., 2012, *ApJ*, **744**, 52
- Perets H. B., Kenyon S. J., 2013, *ApJ*, **764**, 169
- Phinney E. S., Hansen B. M. S., 1993, in *Phillips J. A., Thorsett S. E., Kulkarni S. R., eds, Astronomical Society of the Pacific Conference Series Vol. 36, Planets Around Pulsars*. pp 371–390
- Pichardo B., Sparke L. S., Aguilar L. A., 2008, *MNRAS*, **391**, 815
- Press W. H., Teukolsky S. A., Vetterling W. T., Flannery B. P., 1992, *Numerical recipes in C. The art of scientific computing*. Cambridge: University Press, |c1992, 2nd ed., http://ukads.nottingham.ac.uk/cgi-bin/nph-bib_query?bibcode=1992nrca.book...P&db_key=AST
- Rafikov R. R., 2016a, *ApJ*, **830**, 8
- Rafikov R. R., 2016b, *ApJ*, **830**, 7
- Saladino M. I., Pols O. R., 2019, *A&A*, **629**, A103
- Schleicher D. R. G., Dreizler S., 2014, *A&A*, **563**, A61
- Shakura N. I., Sunyaev R. A., 1973, *A&A*, **24**, 337
- Soker N., 2019, *MNRAS*, **483**, 5020
- Toomre A., 1964, *ApJ*, **139**, 1217
- Vassiliadis E., Wood P. R., 1993, *ApJ*, **413**, 641
- Wang C., Jia K., Li X.-D., 2016, *Research in Astronomy and Astrophysics*, **16**, 126
- Yelverton B., Kennedy G. M., Su K. Y. L., Wyatt M. C., 2019, *MNRAS*, **488**, 3588
- Young M. D., Clarke C. J., 2015, *MNRAS*, **452**, 3085
- de Ruyter S., van Winckel H., Maas T., Lloyd Evans T., Waters L. B. F. M., Dejonghe H., 2006, *A&A*, **448**, 641

APPENDIX A: LOCAL DISC PROPERTIES

Physical quantities can be calculated at a radius R given a disc temperature structure $T = T(R)$. For example, the local disc scale height is,

$$H(R) = \frac{k_B \Gamma}{\mu G M_\star} T R^3, \quad (\text{A1})$$

the sound speed is,

$$c_s(R) = \sqrt{\frac{k_B \Gamma T}{\mu}}, \quad (\text{A2})$$

the density is,

$$\rho(R) = \frac{\Sigma(R)}{H(R)}, \quad (\text{A3})$$

the gas pressure is,

$$P(R) = \frac{k_B T \rho(R)}{\mu}, \quad (\text{A4})$$

the kinematic viscosity (which requires Eq. 5) is,

$$\nu(R) = \frac{\alpha_{\text{disc}} c_s^2(R)}{\Omega(R)}, \quad (\text{A5})$$

the orbital velocity is,

$$v(R) = R \Omega(R), \quad (\text{A6})$$

the local viscous time-scale is,

$$\tau_{\text{visc}}(R) = \frac{R^2}{5\nu(R)}, \quad (\text{A7})$$

and the [Toomre \(1964\)](#) stability parameter, Q , is,

$$Q = \frac{c_s(R) \kappa}{\pi G \Sigma(R)}. \quad (\text{A8})$$

APPENDIX B: DISC INTEGRALS

In this section we provide derivations of the parameters c and m to be used in Eq. 37 when calculating integral properties of the disc.

B1 Angular momentum J_{disc}

The total angular momentum in the disc is,

$$J_{\text{disc}} = \int h \, dM \quad (\text{B1})$$

$$= \int_{R_{\text{in}}}^{R_{\text{out}}} 2\pi h R \Sigma(R) \, dR \quad (\text{B2})$$

$$= 2\pi \sqrt{G M_b} \int_{R_{\text{in}}}^{R_{\text{out}}} \Sigma(R) R^{3/2} \, dR \quad (\text{B3})$$

$$= 2\pi \sqrt{G M_b} \sum_{n=0}^{N-1} \int_{R_{0,n}}^{R_{1,n}} \Sigma(R_{0,n}) \left(\frac{R}{R_{0,n}}\right)^{-2-a_n} R_{0,n}^{3/2} \left(\frac{R}{R_{0,n}}\right)^{3/2} \, dR \quad (\text{B4})$$

$$= \sum_{n=0}^{N-1} \left[2\pi \sqrt{G M_b} \Sigma(R_{0,n}) R_{0,n}^{3/2} \right] \int_{R_{0,n}}^{R_{1,n}} \left(\frac{R}{R_{0,n}}\right)^{-1/2-a_n} \, dR, \quad (\text{B5})$$

i.e. $b_n = -\frac{1}{2} - a_n$ (i.e. $c = -1/2$ and $m = -1$ in Eq. 41) with $i_{0,n} = 2\pi \sqrt{G M_b} \Sigma(R_{0,n}) R_{0,n}^{3/2}$.

B2 Angular momentum flux \mathcal{F}

The total angular momentum flux through the disc is found by integrating the specific torque throughout the disc,

$$\mathcal{F} = \int_{R_{\text{in}}}^{R_{\text{out}}} 2\pi R \Sigma(R) \Lambda(R) dR, \quad (\text{B6})$$

where we assume the specific torque of [Armitage & Natarajan \(2002\)](#),

$$\Lambda(R) = \frac{f_{\text{tid}} q^2 G M_{\text{b}}}{2\Delta^4} \times \begin{cases} R^3 & R < a, \\ a^4 R^{-1} & R > a, \end{cases} \quad (\text{B7})$$

where $q = M_2/M_1 < 1$, $\Delta = \max(H, |R - a|)$ and $f_{\text{tid}} \approx 10^{-2}$. Our disc is thin ($H/R \ll 1$) and typically far from the centre of mass ($R \gg a$) so $\Delta \approx R$ and the torque is as in Eq. 53. The total angular momentum flux is then,

$$\mathcal{F} = \pi f_{\text{tid}} a^4 q^2 G M_{\text{b}} \int_{R_{\text{in}}}^{R_{\text{out}}} \Sigma(R) \times R \times R^{-5} dR \quad (\text{B8})$$

$$= \pi f_{\text{tid}} a^4 q^2 G M_{\text{b}} \int_{R_{\text{in}}}^{R_{\text{out}}} \Sigma(R_0) \left(\frac{R}{R_0}\right)^{-2-a_n} \times R_0^{-4} \left(\frac{R}{R_0}\right)^{-4} dR \quad (\text{B9})$$

$$= \left[\pi f_{\text{tid}} a^4 q^2 G M_{\text{b}} \Sigma(R_0) R_0^{-4} \right] \int_{R_{\text{in}}}^{R_{\text{out}}} \left(\frac{R}{R_0}\right)^{-6-a_n} dR \quad (\text{B10})$$

$$= \pi f_{\text{tid}} a^4 q^2 G M_{\text{b}} \sum_{n=0}^{N-1} \left[\Sigma(R_{0,n}) R_{0,n}^{-4} \right] \int_{R_{0,n}}^{R_{1,n}} \left(\frac{R}{R_{0,n}}\right)^{-6-a_n} dR, \quad (\text{B11})$$

i.e. $b_n = -6 - a$ (i.e. $c = -6$ and $m = -1$ in Eq. 41) and $i_n = \pi f_{\text{tid}} a^4 q^2 G M_{\text{b}} \Sigma(R_{0,n}) R_{0,n}^{-4}$.

B3 Angular momentum flux correction

The flux in Appendix B2 assumes that the disc mass is fixed. We expect to lose mass to both fast and slow processes, where fast means faster than the viscous time-scale and slow means on or slower than the viscous time-scale (Sec. 3.2. Fast processes do not change the angular momentum flux because the material they remove is simply gone, not replaced by the disc spreading. Slow processes on the other hand do change the angular momentum flux, because the disc has time to adjust to fill in the mass that was lost.

To approximate the effect of these slow processes we begin by noting that ([Rafikov 2016b](#)),

$$\frac{d\mathcal{F}}{dh} = \dot{M}, \quad (\text{B12})$$

where $h = \sqrt{GM R}$ is the specific angular momentum of a Keplerian orbit and \dot{M} is the amount of mass passing through the radius R per unit time.

We assume a fixed \dot{M} throughout the disc. We expect this to be a good approximation for X-ray mass loss, which happens primarily near the inner edge of the disc, and it is likewise a good approximation for mass loss through the inner edge of the disc. The correction to the angular momentum flux is then,

$$\delta\mathcal{F} = \dot{M}_{\text{slow}} (h - h_{\text{in}}), \quad (\text{B13})$$

where \dot{M}_{slow} is defined in Eq. 45. Our disc model requires an *average* angular momentum flux, so we integrate this with respect to h in the disc to find,

$$\delta\mathcal{F} \approx \delta\mathcal{F}_{\text{avg}} = \frac{1}{h_{\text{out}} - h_{\text{in}}} \int_{h_{\text{in}}}^{h_{\text{out}}} \delta\mathcal{F}(h) dh = \frac{1}{2} (h_{\text{out}} - h_{\text{in}}) \dot{M}_{\text{slow}}. \quad (\text{B14})$$

B4 Disc total luminosity

The disc luminosity is,

$$L_{\text{disc}} = 2 \int_{R_{\text{in}}}^{R_{\text{out}}} 2\pi R \sigma T^4 dR \quad (\text{B15})$$

$$= \int_{R_{\text{in}}}^{R_{\text{out}}} 4\pi R \sigma T_0^4 \left(\frac{R}{R_0}\right)^{4a_n} dR \quad (\text{B16})$$

$$= \sum_{n=0}^{N-1} \left(4\pi \sigma T_{0,n}^4 R_{0,n} \right) \int_{R_{0,n}}^{R_{1,n}} \left(\frac{R}{R_{0,n}}\right)^{4a+1} dR, \quad (\text{B17})$$

where the factor 2 is because the disc has two sides. The integrand is in the form of Eq. 36 with $b_n = 1 + 4a$ i.e. $m = 4$ and $c = 1$ in Eq. 41, and $i_n = 4\pi \sigma T_{0,n}^4 R_{0,n}$.

APPENDIX C: FITS OF DISC PROPERTIES TO MODEL PARAMETERS

In Figs. C1 and C2 we fit observational properties, y , of our circumbinary-disc model to the model parameters, x (Table 3). In what follows, overbars indicate properties time-averaged over the lifetime of the disc. The disc properties, y , shown from top to bottom are the logarithm of the minimum Toomre Q over the life of the disc, the logarithm of the average ratio of the disc scale height at its outer radius to its outer radius, $\log_{10}(\overline{H_{\text{out}}/R_{\text{out}}})$, the logarithm of the average ratio of the disc scale height at its inner radius to its inner radius, $\log_{10}(\overline{H_{\text{in}}/R_{\text{in}}})$, the outer and inner average radii, $\log_{10}(\overline{R_{\text{out}}/R_{\odot}})$ and $\log_{10}(\overline{R_{\text{in}}/R_{\odot}})$ respectively, the average disc mass, $\log_{10}(\overline{M_{\text{disc}}/M_{\odot}})$, the average disc luminosity, $\log_{10}(\overline{L_{\text{disc}}/L_{\odot}})$, the average binary eccentricity, $\log_{10}(\overline{e})$, the maximum binary eccentricity, $\log_{10}(e_{\text{max}})$ and the disc lifetime, $\log_{10}(t_{\text{disc}}/\text{yr})$. The disc parameters, x , are shown as $\log_{10}(x/x_0)$ where x_0 is our default value of the parameter. We then fit the observable, $\log_{10}(y)$, to a quadratic function in $\log_{10}(x/x_0)$ such that,

$$\log_{10}(y) = \Phi + \mathcal{Y} \log_{10}(x/x_0) + \Theta [\log_{10}(x/x_0)]^2, \quad (\text{C1})$$

where Φ , \mathcal{Y} and Θ are the coefficients shown in each plot.

In many cases, there is little variation of y with x , hence \mathcal{Y} and Θ are small. Our fits are poor when the data bifurcates, e.g. $\log_{10}(e_{\text{max}})$ vs $\log_{10}(\alpha_{\text{disc}})$ or $\log_{10}(f_{\text{id}})$, and in these cases the reader should take care to check Figs. C1 and C2.

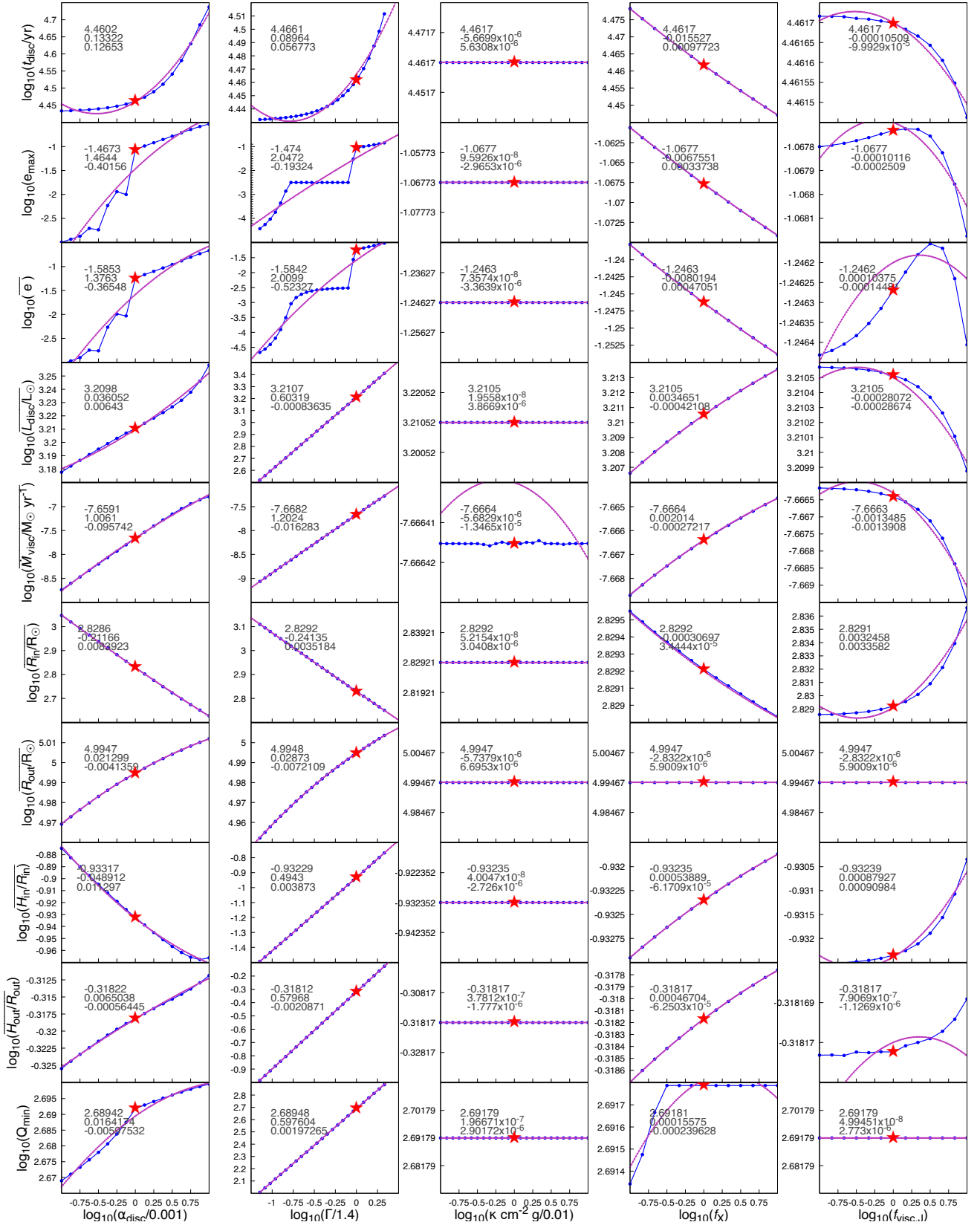


Figure C1. Blue lines show the logarithm of our IRAS08544-4431 disc model properties, $\log_{10}(y)$ where y is (top to bottom) disc lifetime t_{disc} , maximum eccentricity e_{max} , mean eccentricity \bar{e} , disc luminosity L_{disc} , inner-edge mass inflow rate \dot{M}_{visc} , disc inner and outer edge radii R_{in} and R_{out} , scale height ratios at the inner and outer edges $H_{\text{in}}/R_{\text{in}}$ and $H_{\text{out}}/R_{\text{out}}$ and minimum Toomre Q parameter as functions of logarithmic disc parameters, $\log(x/x_0)$: viscosity parameter α_{disc} , gas adiabatic index Γ , disc opacity κ , X-ray disc wind multiplier f_X and inflow viscosity multiplier $f_{\text{visc},i}$, where x_0 is the default parameter shown by the red stars. Overbars indicate values time-averaged over the life of the disc. The coefficients labelled in each plot, from top to bottom, are Φ , Υ and Θ in the fitting function $\log_{10}(y) = \Phi + \Upsilon \log_{10}(x/x_0) + \Theta [\log_{10}(x/x_0)]^2$ shown in magenta.

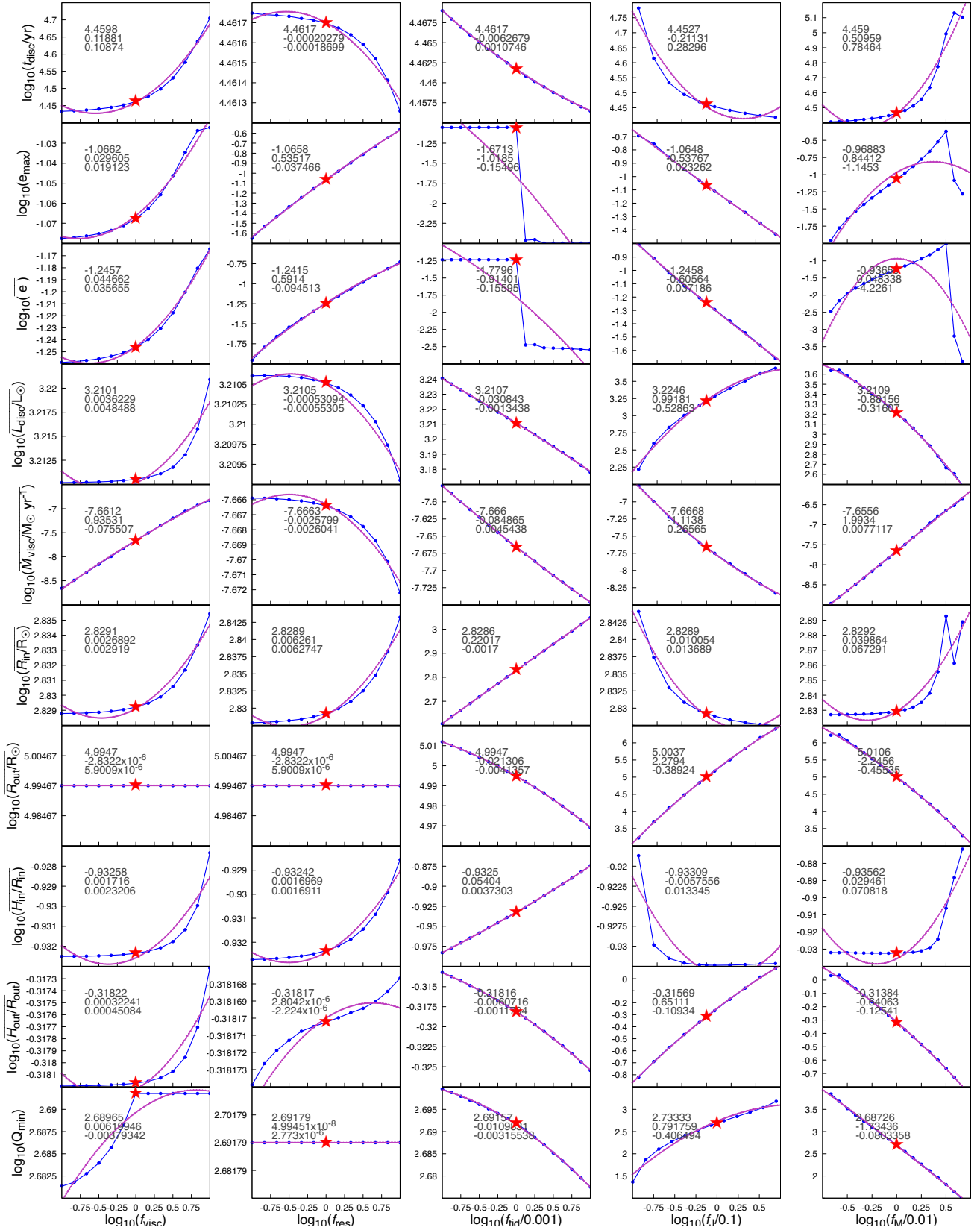


Figure C2. As Fig. C1 but as functions of the viscous-inflow parameter f_{visc} , eccentricity-pumping resonance factor f_{res} , tidal-torque parameter f_{tid} , disc initial angular momentum parameter f_j and disc initial mass parameter f_M .

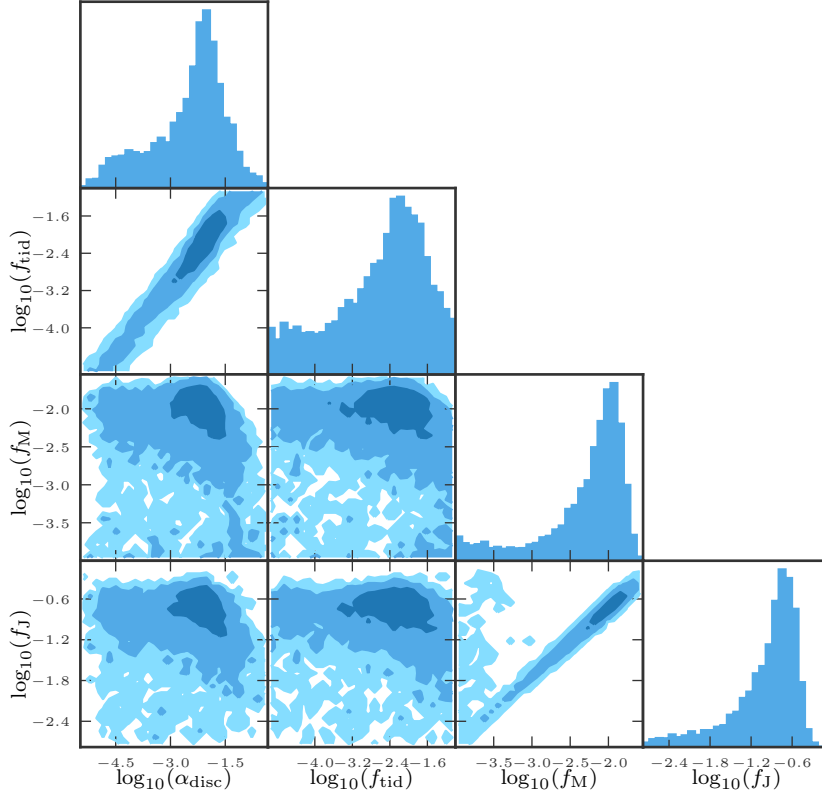


Figure D1. Log-likelihood as a function of model parameters f_M , f_J , f_{tid} and α_{disc} fitted to observations of IRAS 08544-4431 combined with the extra constraints $\dot{M}_{\text{visc}} = 10^{-7} \pm 0.5 \times 10^{-7} M_{\odot} \text{ yr}^{-1}$ and $R_{\text{in}}/a = 2.00 \pm 0.25$. Shades of blue, from darkest to lightest, represent the two-dimensional 1σ , 2σ and 3σ contours.

APPENDIX D: MCMC RESULTS

Figs. D1 and D2 show the log-likelihood as a function of model parameters f_M , f_J , f_{tid} and α_{disc} calculated by comparing our time-averaged disc model to the observations of IRAS 08544-4431 combined with and without conditions on \dot{M}_{visc} and R_{in}/a , respectively, as described in Sec. 4.4. Our Giant-Triangle-Confusograms were created using the `pygtrc` package (Bocquet & Carter 2016).

APPENDIX E: SOLUTION ACCURACY CHECKS

Our solution method (Secs. 2.2 and 2.3) has a maximum theoretical error in disc temperature, $T(R)$, of 32 per cent. We estimate this error in our IRAS 08544-4431 disc solution by rearranging Eq. 11 to,

$$\delta T = \sigma T^4 - \mathcal{A} - \mathcal{B}(1 + C), \quad (\text{E1})$$

and show $\delta T/T$ over the lifetime of our IRAS 08544-4431 model in Fig. E1. The magnitude of $\delta T/T$ is always less than 20 per cent.

In Fig. E1 we also show $\mathcal{D}/[\mathcal{A} + \mathcal{B}(1 + C)]$ to estimate the magnitude of the neglected mass-loss term, \mathcal{D} , which for most of the evolution is negligible, and even near the end of the disc's life when mass loss is greatest, the \mathcal{D} term never exceeds 10 per cent.

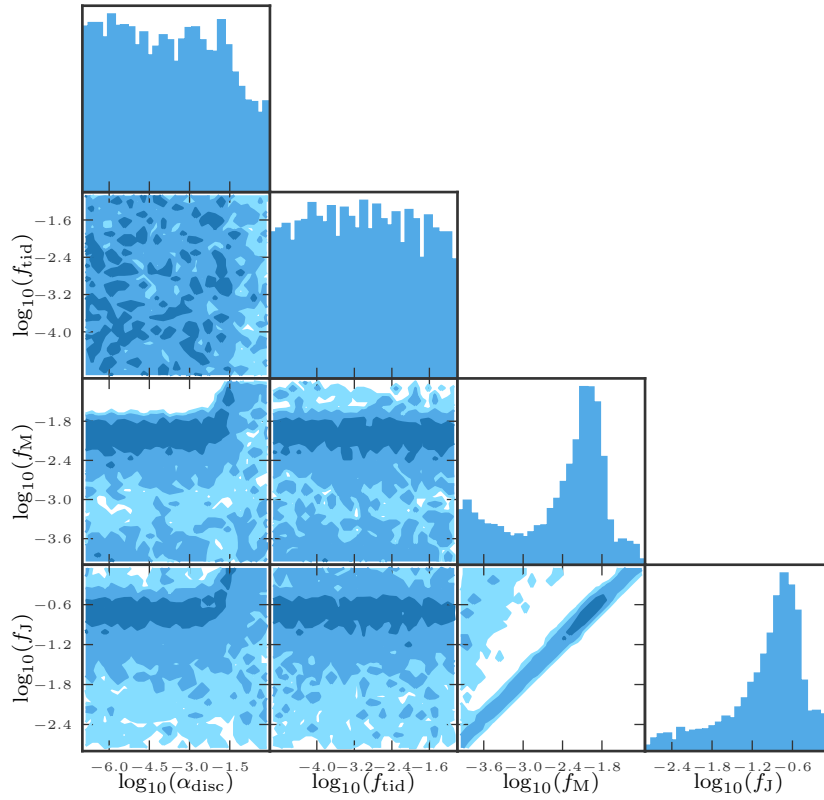


Figure D2. Log-likelihood as a function of model parameters f_M , f_J , f_{tid} and α_{disc} fitted to observations of IRAS 08544-4431 without conditions on \dot{M}_{visc} and R_{in}/a . Shades of blue, from darkest to lightest, represent the two-dimensional 1σ , 2σ and 3σ contours.

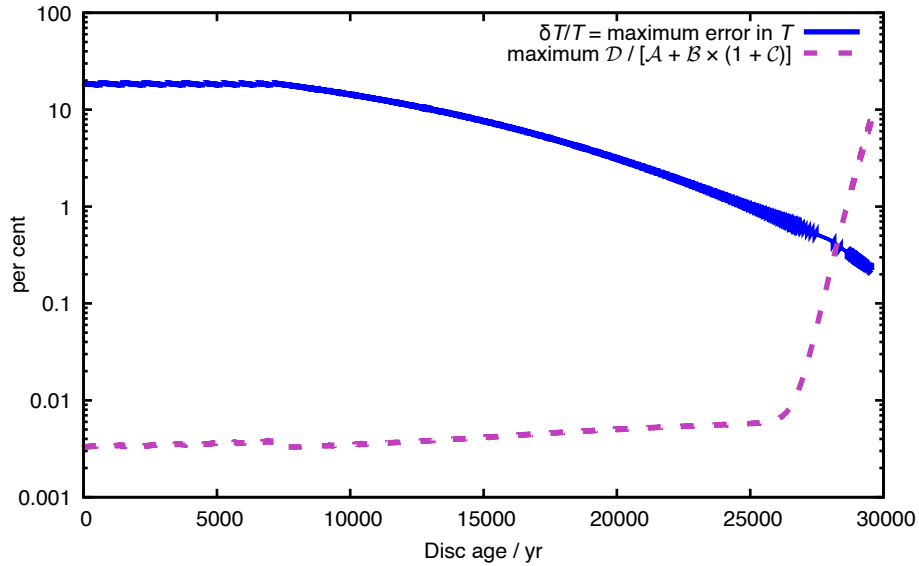


Figure E1. Maximum error in our IRAS 08544-4431 circumbinary-disc temperature solution, $\delta T/T(R)$ (blue, solid line; Eq. E1), and maximum contribution from the mass-loss term, $\mathcal{D}/[A + B \times (1 + C)]$ (magenta, dashed line). At each disc age, the maximum is computed from the values throughout the disc.